Acta Materialia 312 (2026) 122263

Contents lists available at ScienceDirect

Acta Materialia

journal homepage: www.elsevier.com/locate/actamat

Full length article

# Atomistic insights into the enhancement of dynamic yield and fracture responses by chemical short-range order in CoCrNi multi-principal element alloy under quasi-isentropic loading

Zhuocheng Xie [a,b], Wu-Rong Jian [a,b,*], Shuozhi Xu [c], Irene J. Beyerlein [d,e,1], Xiaoqing Zhang [a,b], Ningbo Zhang [f], Xiaohu Yao [a,b,*]

[a] State Key Laboratory of Subtropical Building and Urban Science, South China University of Technology, Guangzhou, Guangdong 510640, PR China
[b] Department of Engineering Mechanics, South China University of Technology, Guangzhou, Guangdong 510640, PR China
[c] School of Aerospace and Mechanical Engineering, University of Oklahoma, Norman, OK 73019, USA
[d] Department of Mechanical Engineering, University of California, Santa Barbara, CA 93106-5070, USA
[e] Materials Department, University of California, Santa Barbara, CA 93106-5050, USA
[f] Key Laboratory of Advanced Technologies of Materials, Ministry of Education, Southwest Jiaotong University, Chengdu, Sichuan 610030, PR China

ARTICLE INFO

*Keywords:*
Dynamic strength
Fracture
Grain boundary-mediated deformation
Chemical short-range order
Multi-principal element alloy

ABSTRACT

Multi-principal element alloys (MPEAs) are emerging as promising structural materials for dynamic environments due to their exceptional mechanical performance. In this study, large-scale molecular dynamics simulations are employed to investigate grain boundary (GB)-mediated plasticity and fracture behavior of nanocrystalline (NC) CoCrNi MPEAs in multi-strain path quasi-isentropic (QI) loading at strain rates ranging from $10^8$ $s^{-1}$ to $10^{11}$ $s^{-1}$. The influence of nanograin size and chemical short-range order (CSRO) on GB deformation mechanisms is systematically analyzed. Compared to chemically random configurations, GBs containing CSRO exhibit reduced energy, suppressed GB-mediated plasticity, and improved stability against dislocation interactions, which weakens the inverse Hall-Petch effect and leads to higher yield strength. CSRO intensity is partially degraded by intragranular dislocation activity in QI compression but partially recovered in subsequent QI tension, and therefore is able to influence void formation and propagation. Under subsequent dynamic tension, CSRO promotes a more uniform dispersion of void embryos and rougher void coalescence paths, which explains its role in increasing the fracture resistance. These findings elucidate the fundamental role of nanoscale chemical ordering in governing the strength-fracture resistance trade-off of NC MPEAs under dynamic loading.

## 1. Introduction

There is no end to the number of automotive, aerospace, energy, and nuclear applications that would benefit from stronger, more damage-tolerant structural materials under extreme impact loading than currently available [1–3]. Particularly, the family of CoCrNi-based multi-principal element alloys (MPEAs) have garnered significant attention for their high Hugoniot elastic limits [4,5], spall strengths [6–8], and toughness [9] under shock loading. MPEAs are a new class of metallic alloys that unlike conventional alloys consist of three or more principal elements [10–12] and to date, not currently used in structural applications. A considerable amount of research has been devoted to characterizing spall strength and damage tolerance for different MPEA compositions and highlighting how they exceed those of a volume-averaged property of their constituents or today's high-performance alloys.

For traditional alloys, which usually contain one principal element, a trade-off often exists between fracture (or spall) strength and damage tolerance (or toughness) [13,14]. In multi-principal element alloys (MPEAs), dynamic loading studies have sought to determine whether chemical complexity can mitigate this trade-off, yet reported trends remain inconsistent. In fine-grained MPEAs subjected to increasing impact velocity, spall strength was found to increase while toughness decreased, with grain-boundary (GB) void nucleation followed by linkage

* Corresponding authors at: Department of Engineering Mechanics, South China University of Technology, Guangzhou, Guangdong 510640, PR China.
*E-mail addresses:* wurong@scut.edu.cn (W.-R. Jian), yaoxh@scut.edu.cn (X. Yao).

[1] Irene Beyerlein was an Editor of the journal during the review period of the article. To avoid a conflict of interest, Irene Beyerlein was blinded to the record and another editor processed this manuscript.

https://doi.org/10.1016/j.actamat.2026.122263
Received 29 August 2025; Received in revised form 16 April 2026; Accepted 19 April 2026
Available online 22 April 2026

into transgranular cracks [9,15]. In contrast, laser-driven shock experiments on CoCrNi reported simultaneous enhancement of spall strength and damage tolerance, which was attributed to nano-recrystallization near the fracture plane and a more homogeneous distribution of incipient voids in nanocrystalline (NC) regions [16]. Meanwhile, high-rate testing of CoCrFeMnNi revealed minimal changes in spall strength and damage accumulation rate relative to lower-rate conditions [17], whereas subsequent experiments demonstrated concurrent increases in strength and toughness when the strain rate was raised from $10^{-3}$ $s^{-1}$ to $6 \times 10^5$ $s^{-1}$ [18], attributed to the activation of nanoscale amorphous regions. These divergent observations suggest that the high-rate response of MPEAs cannot be rationalized by strain rate alone, but is strongly influenced by microstructural attributes, including grain structure, phase stability, and local chemical complexity.

Understanding the reasons for these varied responses and, more generally, the microscopic attributes that control fracture strength and toughness is challenging, since the deformation mechanisms can be different, more intense and/or more sensitive to local, small-scale heterogeneities at elevated strain rates [19]. As in pure metals, post-mortem studies of MPEAs after shock-loading observed that triple junctions of high-angle GBs were preferred sites for void nucleation [7]. Denser dislocation networks and more forest dislocations were generated in the grain interiors (GIs) in dynamic compression tests in Al–CoCrFeNi MPEA systems [20,21] than at lower rates. Higher strain rates have also been found to induce nanotwins in several types of face-centered cubic (FCC) MPEAs [20–24]. Furthermore, the chemical complexity of MPEAs can render them metastable with respect to phase transitions, which can be promoted under the high pressures and large deformations generated in shock loading. The types of phase transitions occurring in high-rate loading ranged from the initial FCC to hexagonal-close packed (HCP) [25], FCC to body-centered cubic (BCC) [26], or FCC-HCP-BCC [27], and, as mentioned, amorphization [16,18]. Secondly, experimental testing and simulations of shock loading caused a heterogeneous, multi-strain path loading state, involving a propagating pressure wave, subsequent reflection wave, and then interacting waves that created a region in the material under extreme tension. Therefore, the void and crack formation processes underlying spall developed after different parts of the material had already experienced varying levels of extreme compression and subsequent tension. This history dependence complicates attempts to unravel the intrinsic contribution of specific microstructural attributes to dynamic strengthening and fracture resistance.

The strong influence of microstructure heterogeneity and chemical complexity on damage nucleation and progression can be investigated in atomic-scale molecular dynamics (MD) simulations of shock loading, albeit at small volumes ($<10^{-3}$ $\mu m^3$) and usually very high rates ($>10^7$ $s^{-1}$). To date, a few MD simulation studies of MPEAs under shock loading have been carried out to identify defect evolution in every stage [28–31]. In MD simulations of FCC CoCrNi-based MPEAs, numerous dislocations, stacking faults (SFs), and nanotwins were observed to form behind the moving shock wave [28,31,32]. In the subsequent release stage, some SFs were removed due to reverse glide. Despite the highly defective GIs left after compression and release, in the final tensile stage, voids still preferred to form at specific GB sites, such as triple junctions. In another work, shock simulations of single-crystal CoCrNi MPEA found that higher shock velocities promoted amorphization in the solid state [29]. Inevitably prevailing at the atomic scale in MPEAs is chemical short-range ordering (CSRO), an atomic-scale chemical heterogeneity, and lattice distortion (LD), an atomic-scale structural heterogeneity [33–39]. In MD simulations of shock-loaded CoCrNi MPEA, CSRO led to the highest Hugoniot elastic limit compared to a random solid solution (RSS) or pure metal bearing nominal properties of the MPEA [28]. CSRO strengthening in this case was rationalized on the basis that both LD and CSRO slow down dislocation propagation, which in turn increased the chances for nanotwinning. CSRO also affected void nucleation. In single crystals and NC material alike, voids preferentially nucleate in the Ni-rich regions. Despite extensive experimental and simulation efforts devoted to understanding the effects of chemical complexity, how deformation history interacts with CSRO to regulate the dynamic strengthening and toughening response of NC MPEAs remains insufficiently understood. In particular, the evolution of CSRO across successive high-rate compression and tension stages, and its impact on yield, damage nucleation and fracture progression, has not been systematically examined.

Much of the complex, inhomogeneous deformation states of the shock process as described above is a consequence of the test method, either gas gun- or laser-driven systems, to stimulate shock, in which deformation is imposed along the loading direction while the rapid loading timescale suppresses lateral stress relaxation [40,41]. In recent years, an alternative dynamic loading condition referred to as a quasi-isentropic (QI) process, has been employed in experiment and MD simulation to represent dynamic high-pressure situations [42–51]. Different from the adiabatic process of shock loading associated with conventional shock testing, QI loading generates large compression deformation with a lower temperature rise. In principle, in QI loading, the material response relies predominantly on the mechanical dissipation associated with microstructural and damage evolution. This facilitates fundamental studies of strength-toughness-microstructure relationships. A recent MD study investigated the response of single crystals CoCrNi MPEAs in very high-rate, high-pressure QI compression [52]. Phase transitions were observed, and the type of phase transition was shown to depend on the orientation of the single crystal. The FCC-to-BCC transformation dominated over the FCC-to-HCP transformation in [100] QI compression. It was revealed that CSRO promoted the BCC transformation in these cases. There was a stronger tendency for amorphization in [110] and [111] QI compression than in the other loading directions.

In this work, using both hybrid Monte Carlo (MC)/MD and large-scale MD simulations, we study the dynamic response of NC MPEAs under the full multi-stage process of dynamic loading, starting with high-rate QI compression followed by a hold, and then finally QI tension to final fracture. The analyses aim to uncover the deformation and fracture mechanisms in every strain path and their connection to yield strength, fracture strength, and failure strain. The focus material is an equiatomic CoCrNi alloy due to its extraordinary strength-toughness balance, especially at cryogenic temperature [53–55], and its tendency to develop CSRO, for which its characteristics have already been well studied. Attention is given to the role of local chemical and structural heterogeneities like CSRO and GBs in the formation and propagation of defects and damage in every stage of the process. The simulations reveal that CSRO simultaneously increases compression yield strength, fracture strength, toughness and lowers void evolution rates.

## 2. Methodology

All MD simulations are conducted using the large-scale atomic/molecular massively parallel simulator (LAMMPS) [56]. The atomic interactions within the Co–Cr–Ni system are described by the embedded-atom method (EAM) interatomic potential developed by Li et al. [57], which has been used since in numerous prior MD studies involving defect evolution within single crystalline [57–62] and NC CoCrNi [63–65].

To build atomic-scale models for the NC CoCrNi, the initial step involves creating NC models of pure Ni. The Poisson–Voronoi tessellation method [66] is used to generate 27 randomly oriented grains for the NC Ni model (*Note* 1 and Figure S1 of the supplementary material). Any atom located within 0.1 Å of a Voronoi cutting plane is excluded from the corresponding grain, in order to eliminate short interatomic contacts between adjacent grains. The influence of the cutoff value is also examined, which does not affect the qualitative conclusions reported in this work (Figure S2). While keeping the grain orientations, shapes, and locations the same, the procedure is repeated to change the

average grain size. Depending on the size selected, which will vary here from 7 to 20 nm, fully periodic cubic systems with side lengths of ~17, 22, 27, 36 and 47 nm are employed, respectively. The total number of atoms in the pure NC Ni samples ranges from 0.5 to 10 million, respectively.

To construct RSS CoCrNi NCs, atoms in the NC Ni sample are randomly replaced by Co or Cr atoms until the desired equal molar composition (Co:Cr:Ni = 1:1:1) is reached. The resulting NCs are referred to as "RSS". To build NCs with CSRO, we employ a hybrid MD and MC simulation scheme with an annealing temperature of 350 K under a variance-constrained semi-grand-canonical (VCSGC) ensemble [59]. Starting with the pure NC Ni model, this scheme exchanges in time two-thirds of the Ni atoms with Co or Cr atoms until the equimolar composition and CSRO are achieved throughout the entire sample, while no compositional constraint is imposed locally within individual grains or GBs. As a result, CSRO and local compositional variations develop naturally across both GIs and interfacial regions. The hybrid MC/MD procedure at 350 K serves as an annealing process to achieve converged CSRO under finite-temperature conditions. The subsequent quenching to zero temperature allows atoms to dynamically rearrange and approach a lower-energy configuration, followed by a static relaxation of energy minimization using the conjugate gradient method to remove thermal vibrations and relax residual atomic forces for subsequent property calculations (e.g., CSRO and stacking-fault energies). Details on the MC/MD methodology can be found in Ref. [59]. Here, we use "SRO" to denote the NC models resulting from this method. Finally, before simulating the QI loading process, all NC models are relaxed at 300 K and zero pressure conditions for 100 ps under the NPT ensemble with three-dimensional periodic boundary conditions (PBCs) to reach an equilibrium state. The final equilibrated configuration is used as the initial state for QI loading, with the stress components fluctuating around zero.

To all NCs, a three-stage QI uniaxial-strain loading is simulated, where in each stage, strain is applied along the $x$ axis and the strains in the other two orthogonal directions are zero. The first stage applies compression at a strain rate of $10^9$ $s^{-1}$ up to a strain level of −0.3, with the atomic positions remapped in the loading direction every time step (1 fs). The rate follows a suggestion of a prior study, which mimics the loading rate of laser-driven shock reaching tens of GPa within tens of picoseconds [67]. The time step in subsequent simulations is maintained as 1 fs for NC samples of different sizes. It should be noted that while affine remapping imposes the macroscopic strain along the loading direction, atomic motion remains dynamically integrated in all three directions using a standard velocity-Verlet algorithm, allowing natural relaxation and dissipative processes to occur. In the second stage, the compressive state is held constant for 100 ps to model defect relaxation during the propagation of the release wave under shock loading. The resulting microstructural rearrangements establish the initial state for the subsequent loading and are reflected in the fracture behavior. In the third and last stage, QI reverse loading is applied using the same deformation protocol as in the first stage, but under a constant tensile strain rate until fracture. The strain rate for this last stage is varied from $10^8$ $s^{-1}$ to $10^{11}$ $s^{-1}$ to identify any strain-rate effects. We did not study the effect of strain rate on compressive loading here because it has been investigated in our prior work [52]. During the whole loading procedure, a micro-canonical ensemble (NVE) is adopted, and the PBCs along all directions are maintained. Here, NVE indicates the absence of any thermostat or heat exchange, while the total energy evolution during QI loading arises from externally imposed mechanical work through homogeneous deformation rather than from thermal control (*Note* 3 and Figure S3 of the supplementary material).

In contrast to shock loading, which brings the material to a final state through a single, abrupt compression front, QI loading describes a continuous deformation process that approximates an isentropic path (Figure S4). Although the absolute strain rates and length scales differ between QI experiments and MD simulations, the loading pressure-specific volume relationship obtained from QI MD simulations closely follows that measured in QI experiments [68] on polycrystalline CoCrNi (*Note* 5 and Figure S5 of the supplementary material), demonstrating that the present QI MD protocol captures the essential near-isentropic thermo-dynamic response of CoCrNi under experimental ramp loading. As a result, for a given stress level, QI loading involves a smaller internal energy increase compared to shock compression, leading to lower temperature states and reduced thermal softening. The evolution of mechanical work $W$ (evaluated from the axial stress and the corresponding volume change along the deformation path) remains physically consistent with the increase of internal energy $\Delta E$ throughout the loading process (*Note* 3 of the supplementary material), which includes both potential and kinetic contributions. The potential energy part accounts for elastic deformation and defect-related configurations, while the kinetic energy part corresponds to the thermal contribution associated with atomic motion. The temperature evolves naturally from the atomic motion which is fully integrated in all three spatial directions, allowing kinetic energy to develop as the result of internal energy redistribution during microstructure evolution (Figure S3).

Visualization of defect evolution and post-processing of the corresponding quantities are based on the adaptive common neighbor analysis (CNA) and dislocation analysis (DXA) method [69] implemented in OVITO [70]. The adaptive CNA determines a local cutoff radius for each atom based on its nearest-neighbor distances, which makes the classification robust against homogeneous elastic deformation during global compression or traction. Atoms that do not match FCC/HCP/BCC templates are categorized as "Others", which include GB atoms as well as highly distorted lattice regions such as dislocation cores, stacking faults and phase transition fronts during deformation. *In-situ* GB atomic potential energy calculation is employed for polycrystal samples after energy minimization. Noncrystalline atoms are first identified as GB atoms by the CNA module, and then per-atom potential energy taken directly from LAMMPS is averaged over all identified GB atoms to obtain the average GB atomic potential energy. This metric is used as an energetic descriptor to compare relative GB energetic states of RSS and SRO models, rather than as a strict thermodynamic GB energy. It should be noted that rigorous evaluation of GB free energies typically relies on thermodynamic integration approaches [71,72], which are beyond the scope of the present work. To identify voids and calculate their surface areas and volumes, the surface mesh algorithm (SMA) [73] implemented in OVITO is employed.

## 3. Results

### 3.1. CSRO distribution in NC

We study NCs with five different average grain sizes: $d$ = 7, 9, 11, 15, and 20 nm, with the intent to increase the GB density. Fig. 1(a) shows the generic NC with $d$ = 20 nm, where atoms with perfect FCC coordination are green and those in the GBs are gray. Atomic configuration analysis of the model classifies gray atoms as "other", lacking FCC, HCP, or BCC structure. As shown in Fig. 1(b), as $d$ reduces from 20 nm to 7 nm, the fraction of atoms in the GB increases accordingly, compared to the interior, taking up a significant fraction of the NC, ranging from 9 to 21%. Cross-sections of two representative grains in the RSS and SRO samples with $d$ = 20 nm are shown in Fig. 1(c). CSRO of Ni-rich regions surrounded by CoCr clusters is observed in the SRO NC, in contrast to the uniform distribution of Co, Cr, and Ni in the RSS NC. The GBs in the same NCs are displayed in Fig. 1(d) with the interior atoms removed. The CSRO in the GBs exhibits a preference for Ni–Ni segregation and CoCr clustering similar to that in its GIs.

Warren–Cowley (W–C) parameters [74,75] are computed atom-wise from instantaneous atomic positions using a radial first-nearest-neighbor (1NN) shell defined by a fixed cutoff distance of 3.0 Å. This

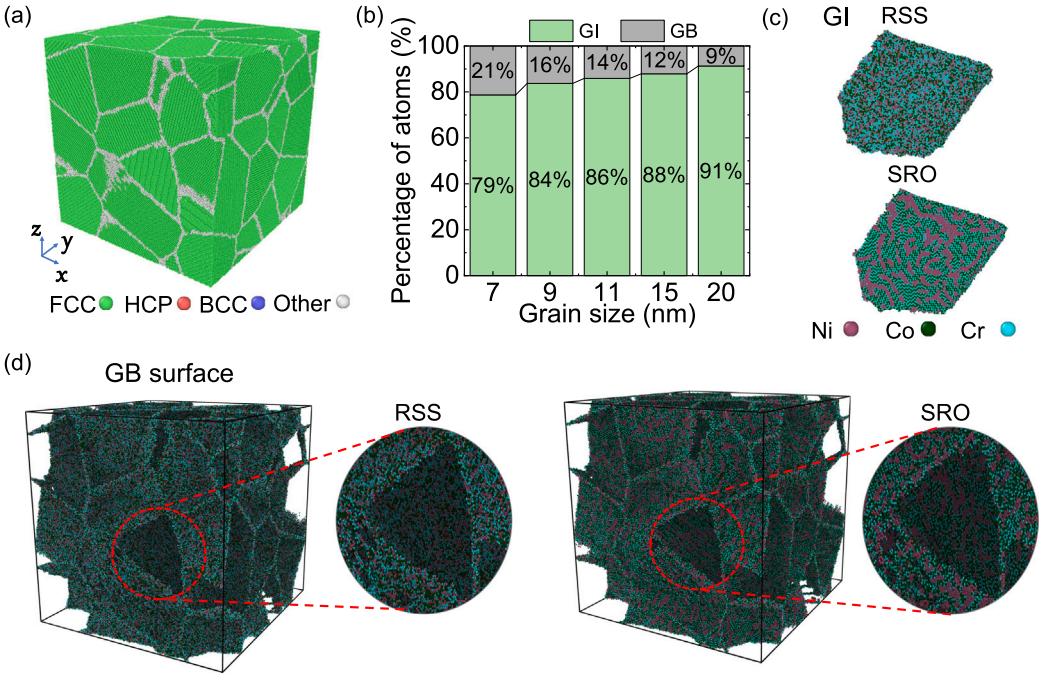


**Fig. 1.** (a) Representative atomic configuration of NC CoCrNi MPEA sample with average grain size of 20 nm. FCC, HCP, BCC atoms, and those with unknown coordination structure are colored green, red, blue, and gray, respectively. (b) shows the percentages of atoms in the GI and GB regions of samples with various average grain sizes. (c) The atomic distribution in the representative grains of the RSS and SRO samples, respectively. (d) The atomic distribution in the GBs of the atomic configuration in (a). Insets show the enlarged view of the chemical disorder/order in the GBs. Here, "SRO" denotes the sample annealed at 350 K during hybrid MD/MC simulations, while "RSS" refers to the sample with an ideally random atomic distribution. (For interpretation of the references to color in this figure legend, the reader is referred to the web version of this article.)

cutoff is chosen to include the first-neighbor peak in the radial distribution function and is verified to capture the 1NN shell for atoms in FCC, HCP, BCC and non-crystalline environments throughout different loading stages (*Note* 6 and Figure S6 of the supplementary material). Therefore, the CSRO metric reported here quantifies local chemical pair correlations within a consistent near-neighbor distance range and is not restricted to a specific lattice topology, enabling unified evaluation in both GI and GB regions. W-C parameters are defined as $\alpha_{ij}^{n} = \frac{p_{ij}^{n} - c_j}{\delta_{ij} - c_j}$, where $n$ is the $n_{\text{th}}$ nearest-neighbor shell of the central $i$-type atom, $p_{ij}^{n}$ denotes the probability of a $j$-type atom being around a $i$-type atom within the $n_{\text{th}}$ shell, $c_j$ is the concentration of $j$-type atoms, and $\delta_{ij}$ is the Kronecker delta function. An $\alpha_{ij}^{n}$ of zero corresponds to a completely random chemical distribution. A positive (negative) $\alpha_{ij}^{n}$ corresponds to a preference of local ordering between pairs of the same, $i = j$ (different, $i \neq j$), species. Larger positive (negative) values for pairs of the same (different) species indicate higher degrees of CSRO. In this work, the first nearest neighbor, i.e., $n = 1$, is used to calculate the W-C parameters.

Fig. 2(a) and (b) show the concentration deviations of Co, Cr, and Ni elements in the GB and GI regions of the RSS and SRO samples with different grain size $d$ compared to the standard equimolar composition. In all RSS samples, the concentration deviations at GBs or GIs from the equimolar composition lay within 1% after thermostat relaxation. All W-C parameters are close to zero (as shown in Fig. 2(c)–(d)), confirming that the model construction procedure sufficiently achieved the target of an ideal random solution. In contrast, a larger concentration deviation is generated in the SRO NCs. In Fig. 2(c)–(d), $\alpha_{\text{NiNi}}^{1}$ exhibits the largest positive value for like pairs and $\alpha_{\text{CoCr}}^{1}$ the largest negative value for unlike pairs among the W-C parameters in both the GIs and GBs. These values indicate local Ni segregation and CoCr clustering, consistent with visual inspection of the SRO models in Fig. 1 and prior MC/MD simulations of this material [57]. Importantly, the GBs of the SRO samples show even higher deviations than the GI, with pronounced differences for $d$ = 7, 9, and 11 nm. As seen in Fig. 2(a) and (b), the GBs have relatively fewer Ni atoms but higher proportions of Co and Cr atoms than the GIs for the same $d$. Consequently, the level of CSRO is slightly lower in the GBs, with $\alpha_{\text{NiNi}}^{1}$ less positive in the GBs. The preference can be understood by comparing the potential energy of the three constituent elements in GBs (Fig. 3). Co exhibits the lowest potential energy in GBs (Fig. 3(b)). Considering further the preference for Cr to bind to Co, the GBs contain a relatively higher proportion of CoCr clusters, and thus reduced $\alpha_{\text{NiNi}}^{1}$.

### 3.2. Response to controlled-deformation QI multi-stage loading

All NC samples exhibit a similar response to the QI multi-stage loading (compression-holding-reverse loading) imposed. Fig. 4 shows the typical evolution of the normal stress component along the applied straining direction throughout the process $\sigma_{xx}$, referred to as the longitudinal stress. In the first stage, the longitudinal stress is negative and hence compressive (Figure S7 and S8). As the other stress components that develop are non-zero and non-negligible (Figure S9), we also analyze the von Mises stress (*Note* 7 in the supplementary material) evolution to reveal the onset of plastic deformation during this stage. In particular, the deviation from linear elasticity in the von Mises stress is defined as the yield strength. Note that the energy-based von Mises stress is inherently insensitive to the sign of individual stress components and the choice of isotropic yield criterion does not alter the mechanistic interpretations drawn from the comparative analysis for RSS and SRO NC samples. Work hardening rate derived from the von-Mises stress–strain curve is used for the analysis of post-yielding behavior (*Note* 8 and Figure S10 in the supplementary material). At the end of the first and second stages, there is no evidence of fracture. In the third stage, when the applied strain is reversed, the compressive longitudinal stress reduces in magnitude more rapidly than it rose in the first stage, a hysteresis that results from the irreversibility of inelastic events that developed in the first stage. The area of the region

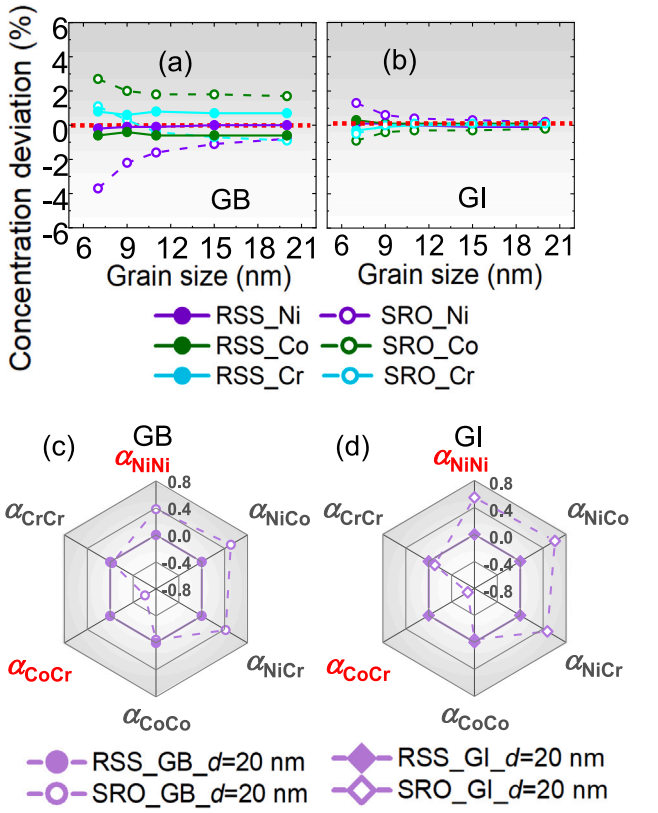


**Fig. 2.** Concentration deviations of Co, Cr, and Ni elements in the (a) GB and (b) GI regions compared to the standard equimolar composition for the RSS and SRO NCs. The pairwise W-C parameters $\alpha_{ij}^{1}$ are calculated for the (c) GB and (d) GI regions in the RSS and SRO NCs with an average grain size of 20 nm. Here, the definitions of models are consistent with those in Fig. 1.

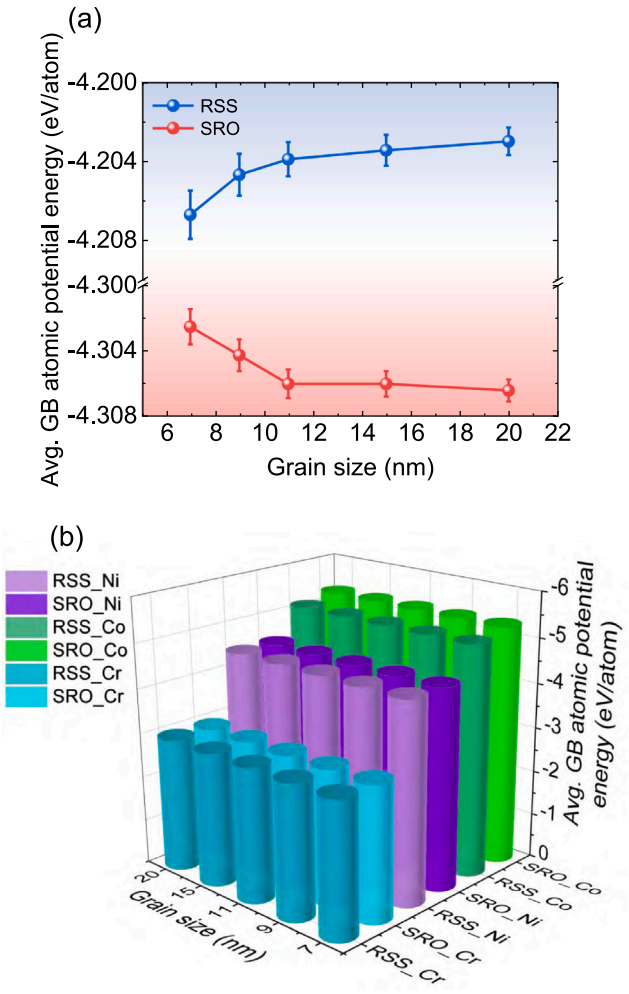


**Fig. 3.** (a) The average GB atomic potential energy and its standard deviation over 100 RSS and SRO samples after energy minimization. (b) The average potential energy of Co, Cr, and Ni atoms at GBs over 100 configurations for each case. The definitions of models are consistent with those in Fig. 1.

bounded by the hysteresis loop denotes the irreversible work during the stage of compressive stress state. As the reverse straining continues, the longitudinal stress becomes tensile, and after some amount of tensile strain, voids are seen to nucleate. Their initiation point can be identified by an initial rise in the void volume fraction (red curve) and void surface area fraction (blue curve) from zero. Specifically, the void volume (surface area) fraction is defined as the total volume (surface area) of all reconstructed voids divided by the instantaneous total volume (surface area) of the simulation box at the same strain state. During the tensile straining period spanning void formation, the longitudinal stress continues to rise until it reaches a maximum value, after which it rapidly drops. The peak value in longitudinal stress is designated here as the fracture strength. With continued straining beyond the fracture strength, the void development transitions from individual formation and growth to void coalescence. For the purpose of comparing NC materials, the strain level at which void growth ends and coalescence begins is defined here as the failure strain. Herein, the area of the region bounded by zero stress line and reverse loading curve until failure strain corresponds to the reverse loading work during the stage of tensile stress state.

To quantify the material's energy absorption under the full QI loading sequence, we define an effective QI toughness as the total mechanical work per unit volume along the actual QI compression-reverse loading path:

$$W_{\mathrm{QI}} = \int_{\mathrm{path}} \sigma \, d\varepsilon.$$

Since the integration follows the real loading trajectory, $W_{\mathrm{QI}}$ naturally includes both elastic storage and the irreversible event through plasticity, which is equal to the sum of the irreversible work and the reverse loading work. This energy-based definition is consistent with the classical interpretation of toughness as the area under the stress–strain curve.

These results demonstrate that the simulated QI process enables exploration of the whole process of inelastic evolution in compression followed by tension up to fracture in NC CoCrNi MPEAs in high-rate conditions. While all NC responses are seen to follow a similar sequence of events, the material properties, such as the yield strength, work hardening, fracture strength, failure strain and toughness generally differ between the RSS and SRO NCs.

### 3.3. Mechanical behavior during QI compression

We first study the effect of CSRO on the first stage of QI compression. Fig. 5 compares the strain evolution of the von Mises stress for the RSS and SRO alloy. The elastic–plastic transition occurs at the strain of around −0.05 (Figure S10) for both alloys at all grain sizes. Fig. 6(a) shows the corresponding yield strengths. CSRO substantially increases the yield strength for all $d$. The yield strengths of both alloys are seen to increase with $d$, which is against the "smaller is stronger" trend, although the effect is weaker for the SRO alloy. This inverse Hall-Petch effect on yield strength is a common observation in MD simulations and in experimental quasi-static tests of FCC NCs and is associated with very fine grain sizes (*Note* 9 in the supplementary

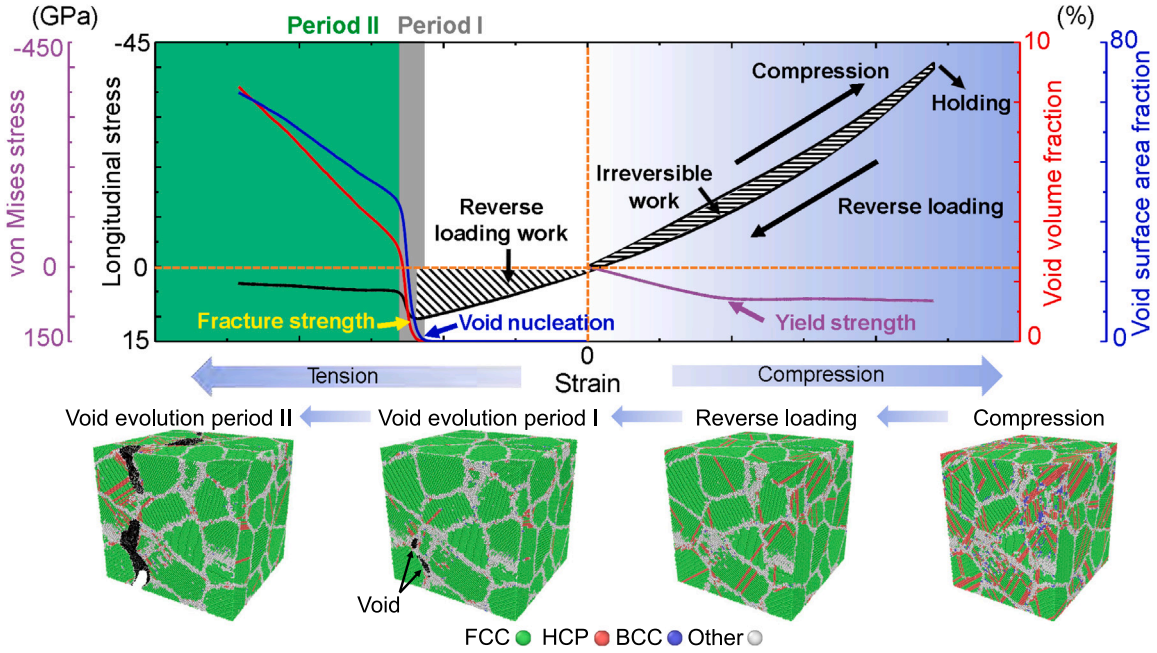


**Fig. 4.** Schematic of the typical macroscopic mechanical response and void failure process under the QI multi-stage loading. The evolutions of longitudinal stress (black curve), von Mises stress (purple curve), void volume fraction (red curve), and void surface area fraction (blue curve) are shown. The plateau in von Mises stress signifies plastic flow during QI compression, with the inflection point from the linear elastic stage to the plastic flow defining the yield strength. The fracture strength corresponds to the maximum longitudinal stress during reverse QI loading. Period I represents rapid void nucleation and embryo growth, while period II reflects void coalescence. The failure strain is the strain at the end of period I/beginning of period II. Dashed horizontal and vertical lines mark zero stress and zero strain, respectively. The area of the region bounded by the hysteresis loop denotes the irreversible work during the stage of compressive stress state, whereas the area of the region bounded by zero stress line and reverse loading curve until failure strain corresponds to the reverse loading work during the stage of tensile stress state. Representative snapshots are shown to illustrate the microstructural features. (For interpretation of the references to color in this figure legend, the reader is referred to the web version of this article.)

material), typically below ~30 nm [76]. It manifests in materials of pure metals and traditional alloys, in monotonic compression as well as tension, and over a range of strain rates. The phenomenon has been associated with diminished dislocation activities within the GIs and greater GB-mediated deformation as $d$ decreases [77,78].

After yielding, the two alloys exhibit vastly different deformation behavior (Fig. 5). The RSS material strain hardens in the first strain hardening stage (WH I), while the SRO material strain softens over WH I (Figure S10). Straining beyond WH I in both alloys results in a second strain hardening stage (WH II), which prevails to the final strain level at the end of the compression ($\varepsilon = -0.3$). Fig. 6(b)–(d) compares the hardening rates in these two stages (WH I and WH II) and onset strain for WH II between RSS and SRO as a function of the grain size $d$. In the SRO alloys, the softening rate in WH I increases with larger $d$ to 11 nm, and larger $d$ delays the onset of the WH II. Moreover, higher hardening rates are observed in the SRO samples than RSS samples in WH II.

### 3.4. Inter- and intragranular plasticity during QI compression

To elucidate the CSRO effect on yield strength, we measure the non-affine displacements and grain rotations at the yield strain of −0.05. The methods for quantifying non-affine displacements and local rotation tensors (*Note* 10 in the supplementary material) in atomic-scale models are described in Refs. [69,79]. Fig. 7(a) compares the average non-affine displacements ($D^2$) in the RSS and SRO alloys for every grain size $d$. The GI displacements in both alloys are similar and insensitive to $d$. The $D^2$ for the GBs, however, is much greater (in some cases at least twice) than that of the GI atoms, influenced by $d$. It should also be noted that, within the inverse Hall–Petch regime, the GB displacement reported here is the average non-affine displacement over GB atoms and thus reflects a local per-atom measure of interfacial rearrangement. As the grain size decreases, the GB volume fraction increases and GB-mediated deformation becomes more significant at the sample scale. Consequently, the average non-affine displacement per GB atom can be smaller in finer-grained samples, even though the overall GB-mediated plasticity is enhanced, consistent with the reduction in yield strength shown in Fig. 6(a). The GB displacements are substantially less in the SRO alloy, with the difference $\Delta D^2$ diminishing with increasing $d$. As shown in Fig. 7(b), both the RSS and SRO alloys exhibit non-negligible grain rotations. The average grain rotation at yielding is much greater in the RSS alloy. The rotation decreases significantly in the RSS alloy with increasing $d$, whereas in the SRO alloy, this same grain size effect is much weaker and even appears to plateau for $d$ greater than 11 nm. Experimental studies of pure FCC NC metals report that smaller nanograins exhibit more pronounced grain rotation [80,81]. This analysis of average local distortions shows that the yield strength is governed by grain rotations and irreversible displacement events at the GBs, for all $d$ studied. The suppressed grain rotation in RSS smaples with larger grain size leads to higher yield strength. CSRO strengthening arises from its effects on constraining GB deformation involving GB displacement and grain rotation. As shown in Fig. 7(c), GB atoms in the SRO samples are predominantly characterized by smaller non-affine displacements, whereas the RSS samples exhibit a higher proportion of larger displacements. The presence of CSRO results in relatively lower GB activities than those occurring in the RSS alloy, thus higher yield strength.

To understand the greater stability of the GBs in the SRO alloys, we calculate the average potential energy of GB atoms in the RSS and SRO alloys prior to loading. Fig. 3(a) shows that the presence of CSRO substantially lowers the GB energy. This stabilization is primarily attributed to the Co element, which is the most prevalent in the GBs in the SRO CoCrNi alloy (Fig. 2(a)) and exhibits relatively low potential energy (Fig. 3(b)).

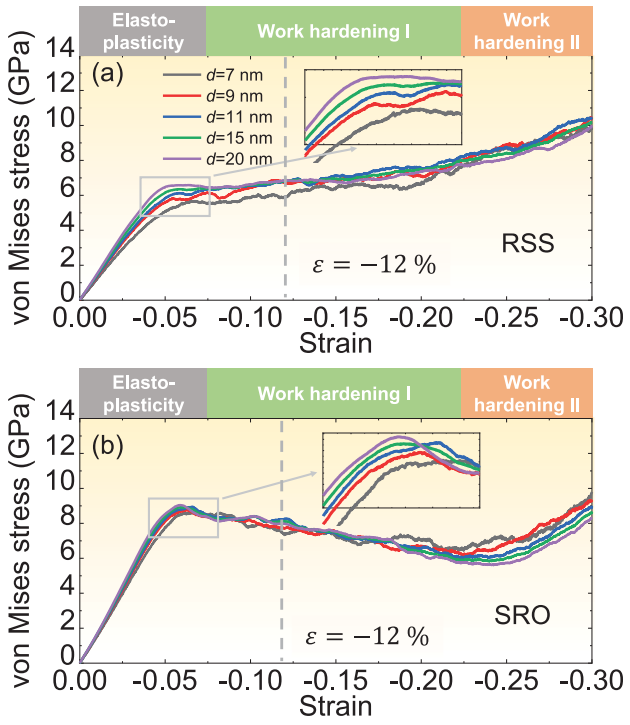


**Fig. 5.** von Mises stress as a function of strain under QI compression for (a) RSS and (b) SRO NC CoCrNi MEAs with varying average grain sizes. Insets highlight the transition from the linear elastic stage to plastic flow in the von Mises stress, marking the onset of dynamic yielding. The vertical gray dashed line denotes the strain of −12%. Three deformation stages are defined based on the work hardening rate derived from the von-Mises stress–strain curve (*Note* 10 in the supplementary material). Here, the definitions of models are consistent with those in Fig. 1.

With increasing strain after yielding, the alloys deform plastically via a series of dislocation slip events and phase transitions. As shown in Fig. 8(a)–(c), within the WH I period, the Shockley partial dislocation density rises in both alloys, even the SRO alloy, wherein strain softening occurs, and at nearly the same rate. The evolutions of non-affine displacements and grain rotations are also tracked. As shown in Figure S11 in the supplementary material, consistent with dislocation activity, GB displacement is enhanced in RSS and SRO alloys with increasing grain size. It should be noted that the smaller GB displacement in SRO samples than RSS alloy indicates a continuous constraint effect by CSRO on GB mobility during QI compression (Figure S11 (a)–(c) and Figure S12). For grain rotation (Figure S11 (d)–(f)), the evolution rates between these two sets of alloys are similar, resembling the trend of Shockley partial dislocation evolution.

To determine whether hardening differences correlate to CSRO-affected phase transitions, we take a closer look at the differences in the evolution of the FCC, HCP, and BCC phases. Fig. 8(d)–(f) compares their evolution, including the unidentifiable "Other" atoms that corresponds primarily to the GBs and secondly to defects apart from Shockley partials and SFs. In the linear elastic region and the elastic–plastic transition, the NCs are FCC. The onset of WH I coincides with the transformation from FCC to either BCC or HCP. The FCC-to-BCC transitions are Bain transformations, and these produce small BCC clusters and occur heterogeneously [82]. The latter FCC-to-HCP transformation corresponds to SF formation from Shockley partial glide and HCP lath production from the formation of SFs on closely parallel planes [83,84]. The growth of the small BCC clusters is limited by the larger-scale displacements from dislocation glide. Over the WH I period, these two phase transformations are, on average, similar between the RSS and SRO alloys.

Stark differences in their WH I hardening/softening rates could alternatively stem from differences in the way defects evolve spatially, details that are lost in averages. Analysis of NC deformation (e.g., Fig. 8(g), (i) and Figure S13) reveals that the SRO grains usually contain one set of intragranular slip bands, whereas the RSS grains develop two or more intersecting slip bands. The preferential formation of coplanar slip bands in SRO grains is facilitated by the decrease in slip resistance due to the destruction of CSRO within each band. This phenomenon has been referred to as "glide plane softening" in conventional binary alloys, and hypothesized to occur in MPEAs with CSRO [85,86]. The predominance of coplanar slip banding has been experimentally reported in this material [53]. Simulations on more traditional FCC alloys have predicted that the intensity of slip bands increases with $d$ in the small grain size regime [87], a trend that aligns with the enhancement in softening rate with larger $d$ seen in Fig. 6(b). The propensity for CSRO to encourage coplanar slip banding over multiple slip banding explains the softening that develops immediately after yield seen in the SRO alloy and not in the RSS alloy, see Fig. 5.

Fig. 8(d)–(f) reveals that WH II corresponds to a marked reduction in the HCP phase. In all NCs, the HCP phase rises in WH I, peaks at a given strain level, and then falls, while the FCC phase continues to drop over WH I and WH II. At the same time/strain level, the BCC phase fraction notably increases at a higher rate than the initial development of BCC clusters at the yield strain. This phase transition sequence from FCC to HCP to BCC (Fig. 8(h) and (j)) has also been experimentally observed in CoCrNi-based MPEAs [88,89] as well as in MD simulations of shock loading and QI compression of single crystals [28,52]. Accordingly, WH II must coincide with an HCP-to-BCC phase transformation. The onset strain of HCP-to-BCC phase transformation is determined as the strain at which the HCP fraction exhibits the first sustained monotonic decrease (Fig. 8 (d)–(f)). The onset strain for WH II in Fig. 6(d) is comparable to that for the HCP-to-BCC phase transformation across all grain sizes and for both RSS and SRO samples (Fig. 8 and Table 1). Specifically, for the RSS NC, the onset of this phase transformation is insensitive to $d$ (consistently occurring at approximately −0.24), while for the SRO NC, it occurs at a lower strain for smaller $d$. Furthermore, Fig. 8(d)–(f) shows that the HCP-to-BCC phase transformation progresses at a much higher rate in WH II in the SRO alloys than the RSS alloys, which aligns with their greater hardening rates in WH II (Fig. 6(c)).

The mechanism underlying the HCP-to-BCC phase transformation in high-rate deformation has been discussed before [27,90]. HCP lath formation involves SF formation on every other {111} atomic planes. New BCC nuclei form when non-coplanar HCP laths intersect and then grow by reactions between intersecting dislocations and the HCP laths. Neighboring BCC embryos coalesce to form the BCC phase. In the SRO NCs here, the enhanced CSRO CoCr clustering at the GBs promoted this phase transition, explaining the grain size dependence in onset strain for WH II not seen in the RSS alloy (Fig. 6(d)). As the BCC phase is the relatively harder phase, the higher rate of transformation would directly correspond to the higher WH rate in WH II possessed by the SRO NC alloys (Fig. 6(c)).

### 3.5. Reverse loading: QI tension

In the last stage of deformation, QI tension is applied after $\varepsilon = -0.3$. After $\varepsilon = -0.3$, a large fraction of the NC has transformed to BCC. However, as seen, during the compression stage, the NCs undergo substantial microstructure evolution with strain, and at lower strains, there is less or no BCC transformed phase. Therefore, we also consider another loading path where QI tension is applied after less QI compression strain $\varepsilon = -0.12$, when the NC has only experienced WH I and its structure is mixed FCC-HCP with little BCC phase. In what

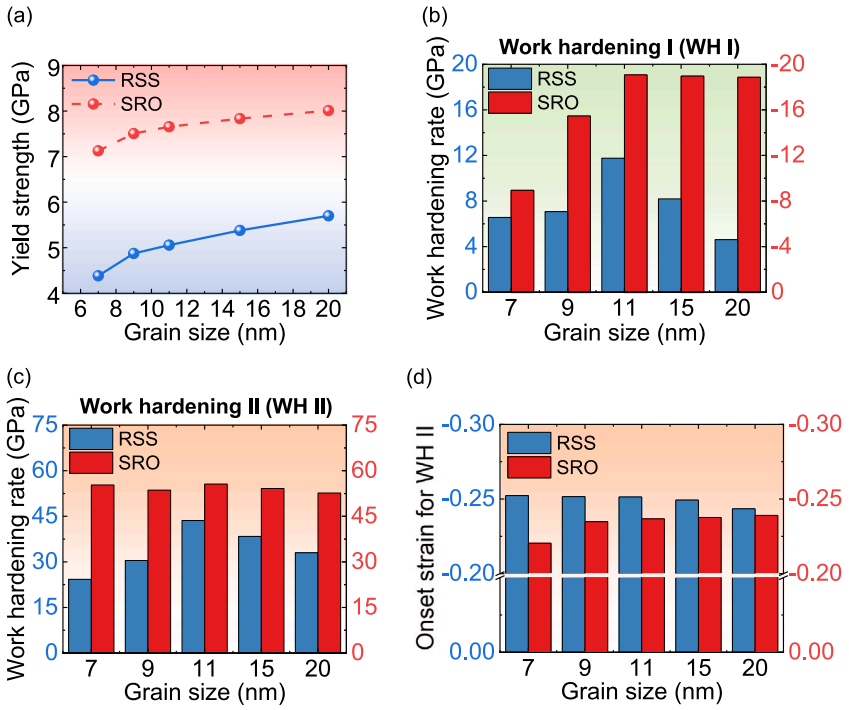


**Fig. 6.** (a) Relation between yield strength and grain size for the RSS and SRO NC CoCrNi samples under QI compression. The average work hardening (WH) rates over the (b) WH I and (c) WH II regimes for each NC sample (*Note* 10 in the supplementary material). The WH rates of the SRO NCs are negative during the WH I regime, corresponding to strain softening. (d) Onset strain for WH II.

**Table 1**
Onset strain for HCP-to-BCC phase transformation and WH II.

| Onset strain for HCP-to-BCC/WH II / MPEA \ Grain size (nm) | 7 | 9 | 11 | 15 | 20 |
|---|---|---|---|---|---|
| RSS | −0.235/−0.252 | −0.240/−0.252 | −0.240/−0.251 | −0.240/−0.249 | −0.240/−0.245 |
| SRO | −0.200/−0.220 | −0.205/0.235 | −0.210/−0.236 | −0.220/−0.237 | −0.230/−0.239 |

follows, the choice of two loading paths aims to examine the effect of the BCC transformed phase on subsequent fracture behavior.

Fig. 9(a)–(d) shows the phase evolution in a representative region of the NCs under reverse loading. As the compressive strain decreases, we observe a reverse transformation of HCP to FCC in the SRO alloy in loading path 1 (lp1) with compression prestrain of $\varepsilon = -0.12$ and to a minor extent in the RSS alloy. In loading path 2 (lp2), we observe a reverse transformation from BCC to HCP after the full prestrain of $\varepsilon = -0.3$ in both alloys. Considering the multiple and large-strain path history experienced by these NCs, whether CSRO would have a lasting effect on the behavior in these final stages of tensile strain is worth detailed analysis.

As defined in Fig. 4, period I represents rapid void nucleation and embryo growth, while period II reflects void coalescence. We first compare the fracture strength between RSS and SRO NC samples under identical grain size and strain-rate conditions, where fracture strength is defined as the peak longitudinal tensile stress occurring during period I. The results for all $d$ and strain rates are shown in Fig. 10. For lp1, SRO samples consistently exhibit higher fracture strength than their RSS counterparts at low strain rates, indicating that CSRO-induced strengthening persists even after the substantial microstructural evolution induced by QI compression and reverse loading. This strengthening effect is most pronounced at the lowest strain rate ($10^8$ $s^{-1}$), particularly for larger grain sizes. In contrast, for lp2, the difference between RSS and SRO samples is negligible across all grain sizes and strain rates, suggesting that the CSRO strengthening effect becomes suppressed under this loading condition. Moreover, fracture strengths are consistently lower for lp2 than for lp1 under identical conditions.

For the strain-rate effect, at high strain rates ($\geq 10^{10}$ $s^{-1}$), the fracture strength becomes relatively insensitive to grain size and CSRO, indicating rate-dominated behavior. However, at lower strain rates ($10^8$–$10^9$ $s^{-1}$), microstructural features play a more significant role, which is manifested by the grain size effect. In both RSS and SRO samples, fracture strength increases as grain size decreases at $10^8$ $s^{-1}$ in both lp1 and lp2 (Fig. 11(a)–(b)), reflecting grain-size strengthening under reverse loading.

Next, we compare the failure strain between RSS and SRO samples, defined as the tensile strain at the end of period I, corresponding to the onset of excessive void coalescence. While failure strain is conventionally associated with complete separation or void percolation, we adopt the strain at which rapid void coalescence begins, since this marks the onset of loss of load-carrying capacity in the simulations. The comparison between RSS and SRO systems is shown in Fig. 11(c)–(d) for the two lowest strain rates ($10^8$ and $10^9$ $s^{-1}$), where microstructural effects are most pronounced. For lp1, the failure strain of SRO samples is comparable to or slightly lower than that of RSS samples across all grain sizes. A similar trend is observed for lp2. Thus, although CSRO enhances fracture strength under certain conditions (Fig. 11(a)–(b)), it does not lead to a systematic increase in failure strain.

Note that the failure strain is also related to grain size. At strain rates of $10^8$ and $10^9$ $s^{-1}$, smaller grains generally exhibit slightly higher

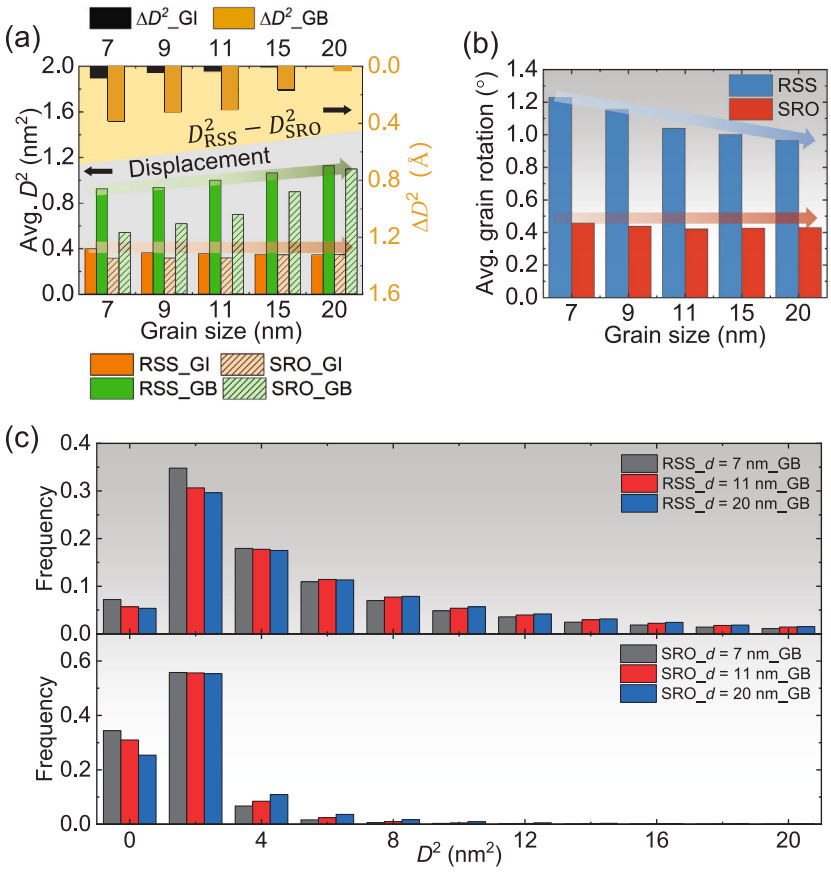


**Fig. 7.** (a) Average non-affine displacement ($D^2$) per GB and GI atom within each NC and (b) average relative grain rotation of 27 grains at the yield point during QI compression. The difference in $D^2$ between RSS and SRO alloys is presented as $\Delta D^2$ in (a). (c) Frequency distribution of $D^2$ for GB atoms within different NC models.

failure strains, suggesting delayed void coalescence in finer microstructures. Increasing strain rate reduces the sensitivity of failure strain to grain size, indicating a transition toward rate-dominated fracture behavior.

To elaborate the CSRO effect on fracture resistance, toughness consisting of irreversible work and reverse loading work is calculated for RSS and SRO samples with respect to different loading paths, as shown in Fig. 12. It is clear that larger plastic dissipation is produced in SRO samples during the compression stage along lp1 and lp2 for different grain sizes, which is mainly attributed to the higher energy penalty in case of dislocation glide and the formation of planar faults. Moreover, the reverse loading work decreases with increasing grain size for both RSS and SRO samples due to the decreasing fracture strength and failure strain of larger grain sizes. In spite of divergent microstructural evolution during two loading paths, SRO still shows considerable toughening effect in the material, especially along lp2. When strain rate further increases over $10^{10}$ $s^{-1}$, the SRO toughening effect becomes weaker since the strain rate effect is predominant during deformation (Figure S14). Taken together, the results in Figs. 6(a), 10(a) and 12 demonstrate that CSRO enhances both the dynamic yield strength and fracture strength, while maintaining enhanced toughness under low strain rates. This indicates that dynamic strengthening is achieved without sacrificing toughness.

To understand how CSRO influences these tensile properties, we return to the start of reverse loading and examine the phase transitions that ensue. For $10^8$ $s^{-1}$, Fig. 9(e)–(j) shows the development of the FCC, BCC, and HCP phases during reverse loading up to a tensile strain of 0.1. For lp1, distinct evolution of microstructures is observed in reverse loading for the RSS and SRO NCs. In the RSS NCs, the dislocation and SF networks remain largely confined within the GIs (Fig. 9(a)–(b)). The HCP content in the RSS NCs only moderately changes with decreasing compressive strain. In contrast, the SRO NCs deform by the absorption of dislocations and SFs by GBs (Fig. 9(a)–(b)). Unlike the RSS alloys, the fraction of HCP structure decreases with diminishing compressive strain in the SRO alloys (Fig. 9(e)–(g)). The SRO NCs nearly recover the FCC state when the strain becomes tensile, which is not the case for the RSS NCs.

For lp2, as the compressive strain reduces, the BCC structure fully transforms into the HCP structure for both alloys (Fig. 9(c)–(d)). As the reverse straining continues, the HCP structure transforms back to FCC, but only partially up to the point of void formation. More FCC structure is recovered in the SRO NCs than RSS NCs (Fig. 9(h)–(j)). The effect of CSRO on fracture strength and toughness can therefore be attributed to differences in the proportions of HCP phase and not to any retained BCC phase. CSRO leads to less HCP phase in the NCs at the point when deformation turns tensile.

Thus far, we have seen that CSRO impacts tensile properties, and before the point of tensile failure, the alloys experience ample local displacements and phase changes. The CSRO is known to change during deformation, as dislocation activities continually shift planes and the grains rotate [81,91]. The expectation is that after the accumulation of irreversible slip events over large straining periods, the CSRO would be destroyed and irrecoverable even if the applied loading were removed or reversed. The W-C parameters that measure CSRO levels can be defined for all phases at any time/location in the NCs. Fig. 13 plots the evolution of the pairwise CSRO parameters, $\alpha^1_{NiNi}$ and $\alpha^1_{CoCr}$, during

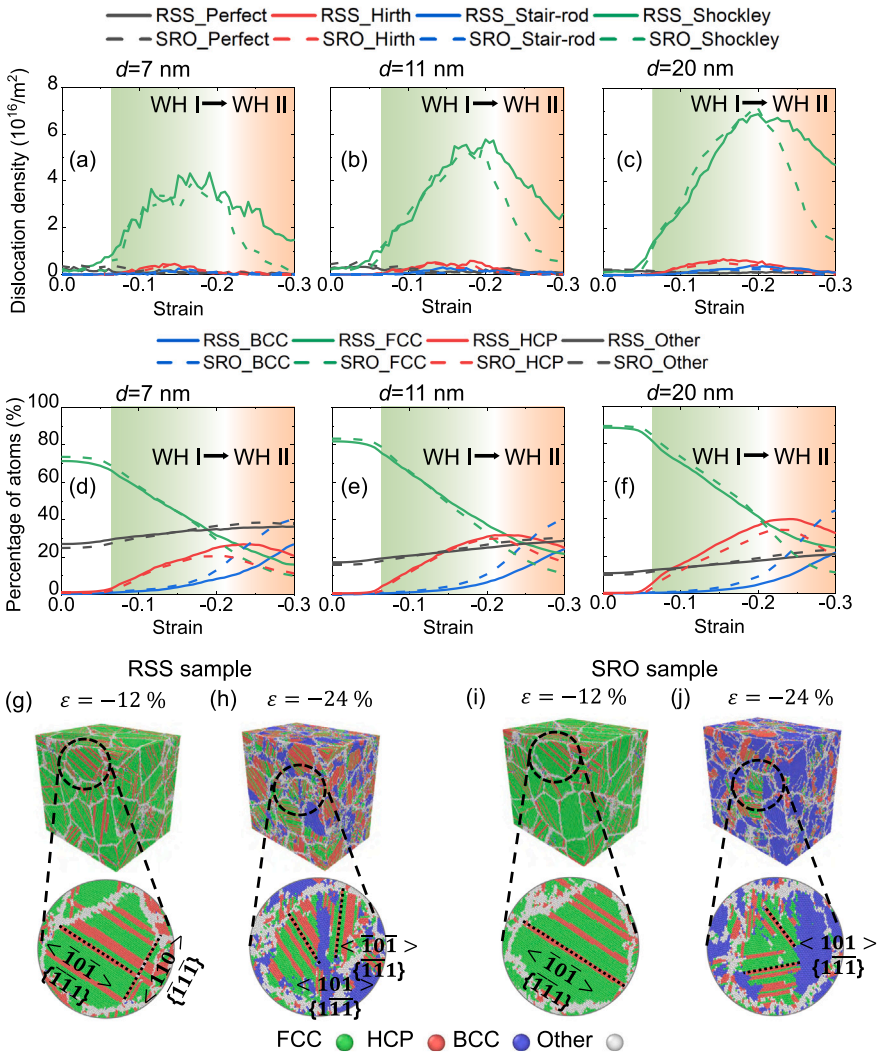


**Fig. 8.** (a)–(c) GI dislocation density development and (d)–(f) crystalline structure evolution in the RSS NC (solid lines) and SRO NC (dashed lines) samples during QI compression. The two WH regimes are consistent with those in Fig. 5. Atomic configurations at different compressive strain levels during QI compression for (g)–(h) RSS and (i)–(j) SRO NCs with an average grain size of $d$ = 20 nm. Here, the atomic coloring of crystalline structure and the definitions of models are consistent with those in Fig. 1. (For interpretation of the references to color in this figure legend, the reader is referred to the web version of this article.)

the entire QI process for lp1 and lp2 in the SRO NCs. During the QI compression stage, increasing intensity of microstructure evolution, such as Shockley partial dislocation glide, SF formation, and phase transitions, causes the absolute values of the CSRO parameters to gradually decrease. This reduction occurs because Shockley partial dislocation-CSRO interactions disrupt CSRO, lowering the proportion of locally ordered regions. With the dominant role of Shockley partial dislocation during QI compression (Fig. 8(a)–(c)), the reduction in CSRO by the leading Shockley partial changes the local stacking fault energy (SFE), which lowers the attractive force between the two partial dislocations. The different SFEs during QI compression and reverse loading lead to an asymmetric microstructure response of these two stages under different loading paths (Figs. 8 and 9). Upon reversing loading in lp1 (Fig. 13(a)), the CSRO parameters exhibit partial recovery. Remarkably, the reversibility of CSRO demonstrates its potential to reduce in one load path and to regain when the sense of loading is reversed. Such reversibility suppresses excessive plastic dissipation (Fig. 9(a)–(b)) and enables sustained reverse loading work until fracture (Fig. 12). In contrast, in lp2, the CSRO parameters do not recover, and the substantially reduced CSRO present after $\varepsilon = -0.3$ is maintained even after complete reverse loading and, importantly, at the point when void nucleation begins (Fig. 13(b)). Yet, CSRO still persists (i.e., the W-C parameters are non-zero) after lp2, albeit at a reduced level. Any CSRO strengthening effects on fracture strength and toughness will simply be weaker after lp2 compared to lp1. This explains the weaker CSRO effects on fracture strengths and failure strains measured after lp2 compared to lp1, seen in Fig. 11. It should also be noted that global CSRO parameters in Fig. 13 are computed as the average of atom-wise W–C parameters evaluated using the first-nearest-neighbor shell for each atom in the current atomic configuration. The local destruction of CSRO is possible to be compensated by the reconstruction of CSRO through dislocation glide along two opposite directions, which mitigates the overall reduction of CSRO parameters. Nevertheless, it shows the effect of loading history on CSRO development, thus indicating the characteristic of rejuvenation in the material.

The CSRO that develops in CoCrNi alloy facilitates the transition from HCP to FCC in reverse loading. Since the HCP-to-FCC phase transformation occurs by SF contraction and reverse Shockley partial glide, the elevated SFE (Figure S15) reduces the energy barrier for the HCP-to-FCC reverse transformation [53,57,92].

### 3.6. Void evolution during dynamic fracture

Considering the presence of CSRO and the large differences in CSRO between lp1 and lp2, we study the role of CSRO in void nucleation and

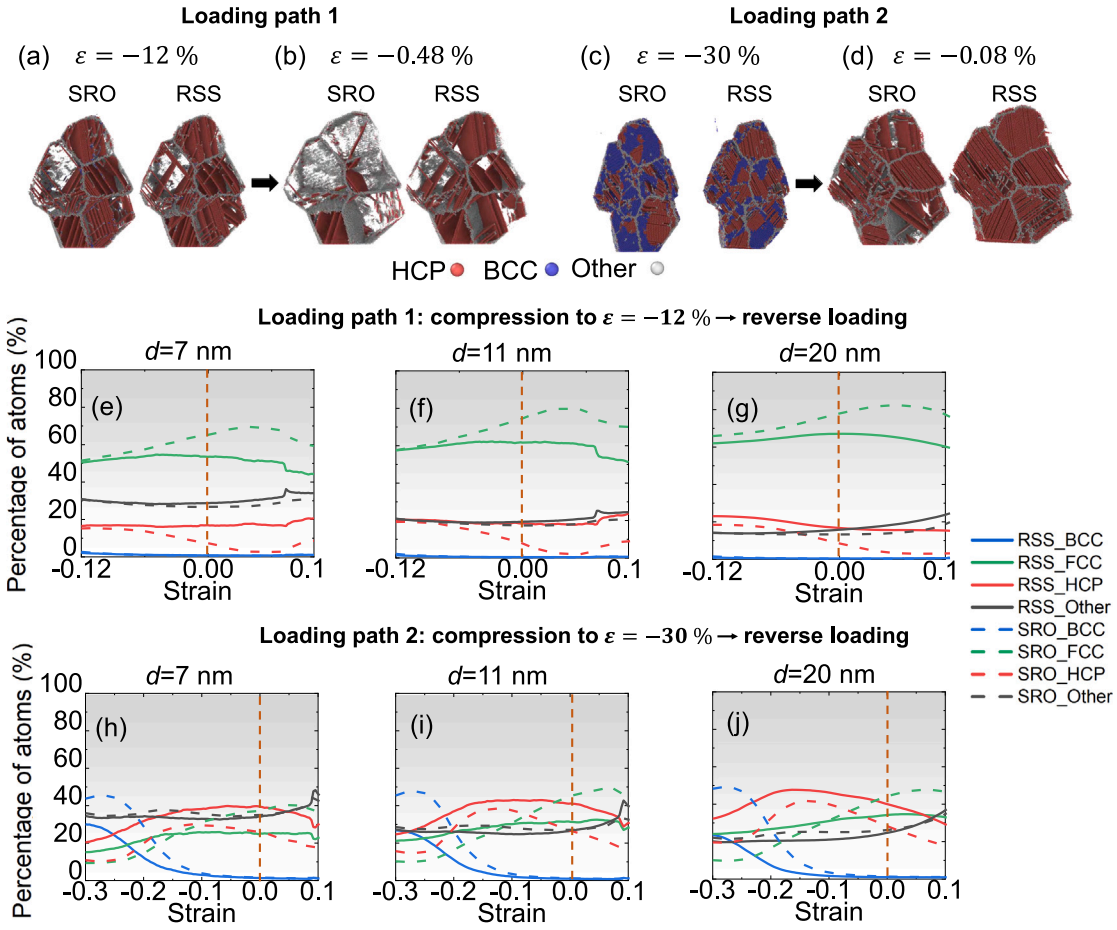


**Fig. 9.** Microstructural evolution of the local grains within the RSS and SRO samples with the average grain size of 20 nm: (a)–(b) for the reverse loading during loading path 1 and (c)–(d) for the reverse loading during loading path 2. The FCC matrix is deleted for better visualization of GI defects. Evolution of microstructures with varying grain sizes: (e)–(g) for the reverse loading during lp1 and (h)–(j) for the reverse loading during lp2. A strain rate of $10^8$ $s^{-1}$ is applied for reverse loading. Specifically, vertical dash lines denote the moments of zero strain during lp1 and lp2, respectively. Here, the definitions of models follow Fig. 1.

growth in periods I and II. For the lowest strain rate $10^8$ $s^{-1}$ and lp1, Fig. 14(a) and (b) compare the time evolution of the void volume fraction and void surface area fraction between the RSS and SRO alloys from the start of period I, which occurred at about the same strain. Voids initiate earlier in the SRO alloys than in the RSS alloys. A similar finding is observed for the rate $10^9$ $s^{-1}$ and lp2 (Figure S16–S17).

To understand how CSRO promotes early void nucleation and influences void growth, void formation in three-dimensional (3D) space is examined. We compare the time evolution of void development spatially in the RSS and SRO NCs over the period I by identifying only void surface atoms with Voronoi volumes exceeding 20 $Å^3$. In both NCs, void nucleation begins at the GBs. Spatial maps show distinct differences in the distribution of void embryos. In the RSS alloy, fewer voids form, and failure progresses by the expansion of a few dominant voids. Their growth is relatively rapid (Fig. 15(a)). In contrast, in the SRO NC, more voids nucleate, and their nucleation sites are randomly distributed throughout the GBs. Coalescence of neighboring void embryos in the SRO NCs results in irregular voids with larger surface areas compared to those in the RSS NCs (Fig. 14(b), Fig. 15(b) and Figure S18). To compare this rugged progression of void growth with the monotonic growth progression seen in the RSS alloy, the void evolution rate derived from the slope of the void volume fraction curve in period I is calculated. For a given deformed sample, a larger surface area corresponds to a higher surface area fraction, indicating more tortuous or rugged void morphology. In SRO samples, this increased geometric complexity delays rapid void growth during period I, and thus the voids in the SRO NCs have a significantly reduced void evolution rate compared to the RSS NCs, as shown in Fig. 14(c). The remarkable differences in void progression caused by CSRO can explain the higher fracture strengths measured in the SRO alloy during lp1.

CSRO promotes void nucleation and thus, much of the robustness to dynamic fracture afforded by CSRO must rely on another factor. Based on the 3D mapping of void growth, greater fracture strengths and comparable failure strains appear to rely instead on a high level of spatial uniformity in void formation. To quantify the spatial heterogeneity in voids for the entire sample and better elucidate the CSRO effect, we adopt the local heterogeneity parameter $h$ [93]. The simulation box is partitioned into $2^{3k}$ cubic grids at subdivision level $k$, and the distribution of void-surface atoms is evaluated across these grids. The parameter $h$ is defined as

$$h = \frac{1}{2S}\sum_{k=1}^{r}(8.89)^{1-k}\sum_{i=1}^{2^{3k}}\left|m_i - \overline{m}(2^{3k})\right|, \tag{1}$$

where $S$ is the total number of atoms on the void surfaces, as before identified as atoms with a Voronoi volume exceeding 20 $Å^3$. The quantity $\overline{m}(2^{3k})$ denotes the average number of void-surface atoms per grid at level $k$, and $r$ is chosen such that each grid contains at most one atom. The parameters $\overline{m}$ and $m_i$ represent the average atom number per grid (ranging from 0 to 1) and the actual atom number in the $i$th grid (either 0 or 1), respectively. For an ideally uniform

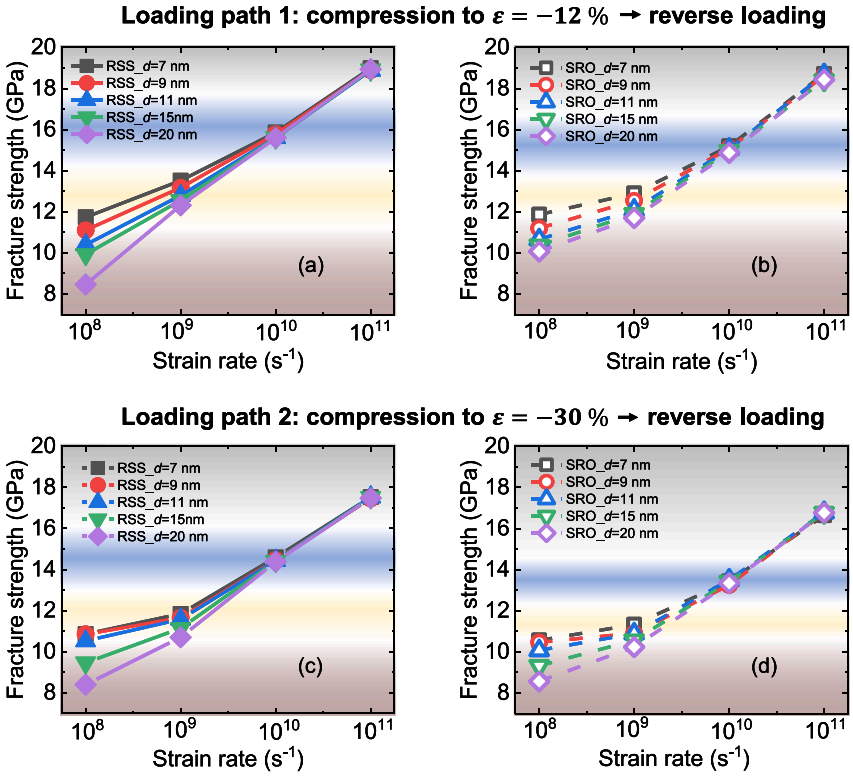


**Fig. 10.** Dependence of fracture strength on strain rate in the RSS and SRO NCs with varying grain sizes during reverse loadings of (a)–(b) loading path 1 and (c)–(d) loading path 2.

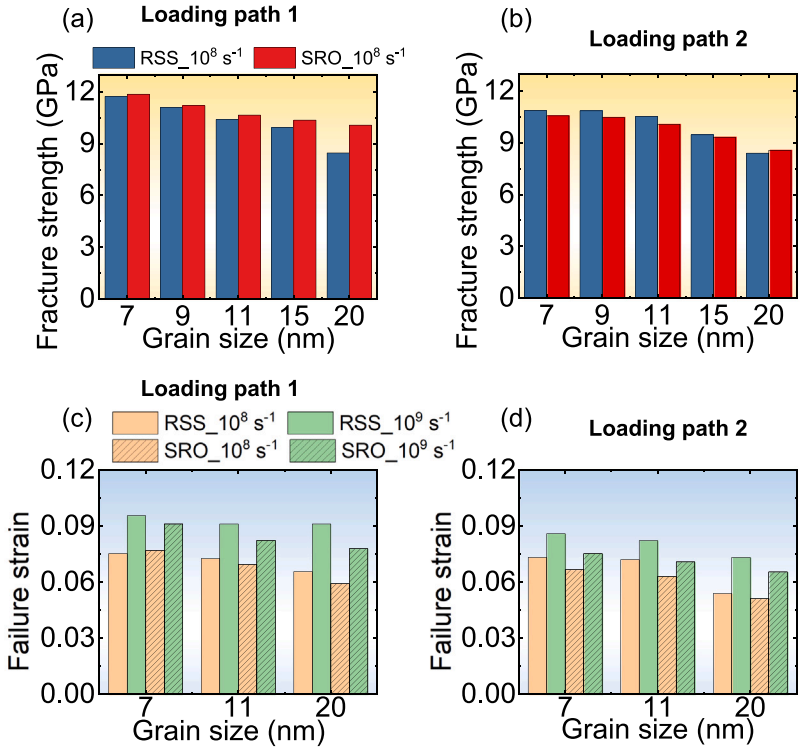


**Fig. 11.** (a)–(b) Fracture strength (the maximum tensile stress along the loading direction) at $10^8$ $s^{-1}$ and (c)–(d) failure strain (the tensile strain at the end of period I) for samples with varying grain sizes during lp1 and lp2, respectively.

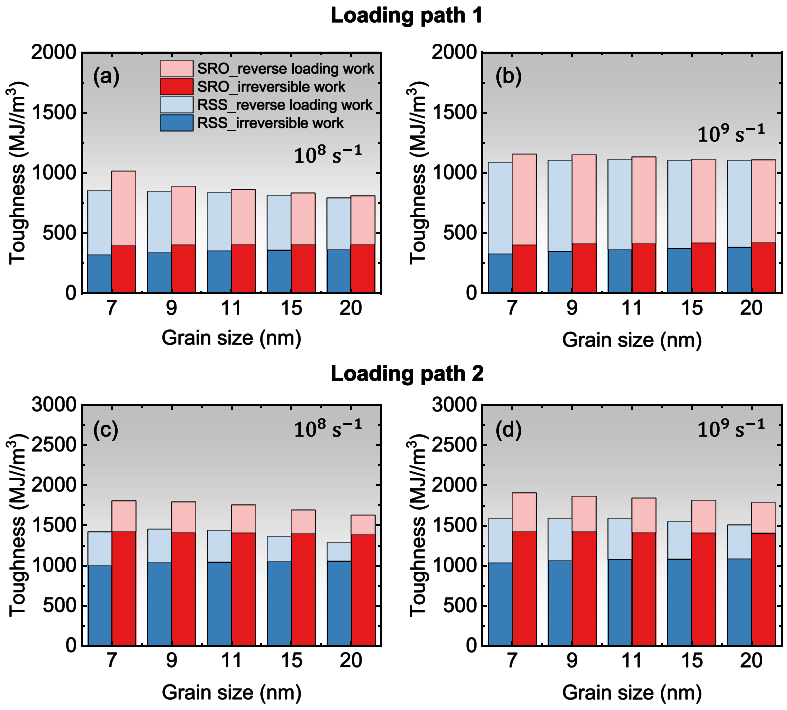


**Fig. 12.** Toughness as the sum of irreversible work and reverse loading work for NC samples with varying grain sizes during (a)–(b) lp1 and (c)–(d) lp2, respectively.

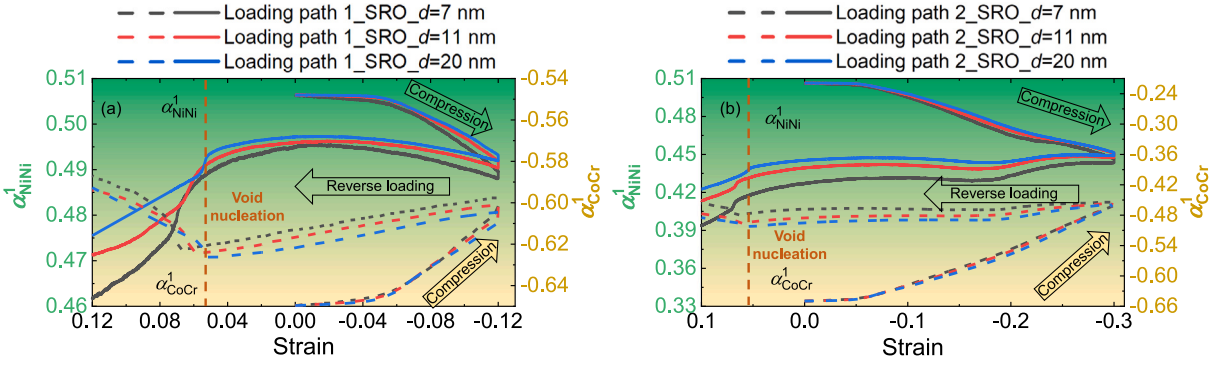


**Fig. 13.** Evolution of pairwise CSRO parameters $\alpha^1_{\mathrm{NiNi}}$ and $\alpha^1_{\mathrm{CoCr}}$ in SRO NCs with varying grain sizes during (a) loading path 1 and (b) loading path 2, respectively. Specifically, solid lines denote $\alpha^1_{\mathrm{NiNi}}$ and dash lines indicate $\alpha^1_{\mathrm{CoCr}}$. Vertical dash lines denote the critical tensile strains for void nucleation. Here, the definitions of models follow Fig. 1.

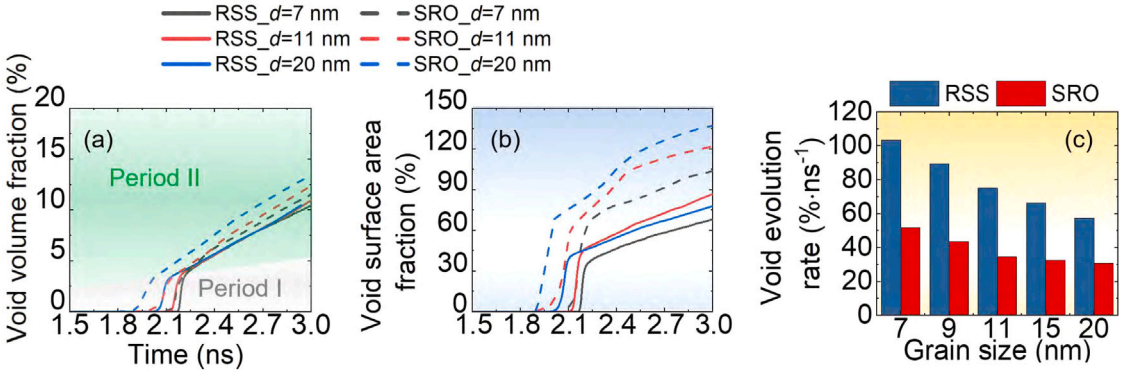


**Fig. 14.** Evolution of (a) void volume fraction and (b) void surface area fraction in the RSS and SRO NCs at a strain rate of $10^8$ s$^{-1}$ during the reverse loading of lp1. In (a), two distinct periods of void evolution are identified based on the slopes of the void volume fraction curves. (c) Void evolution rate over period I, derived from the slope of the void volume fraction curve in (a) using linear fitting.

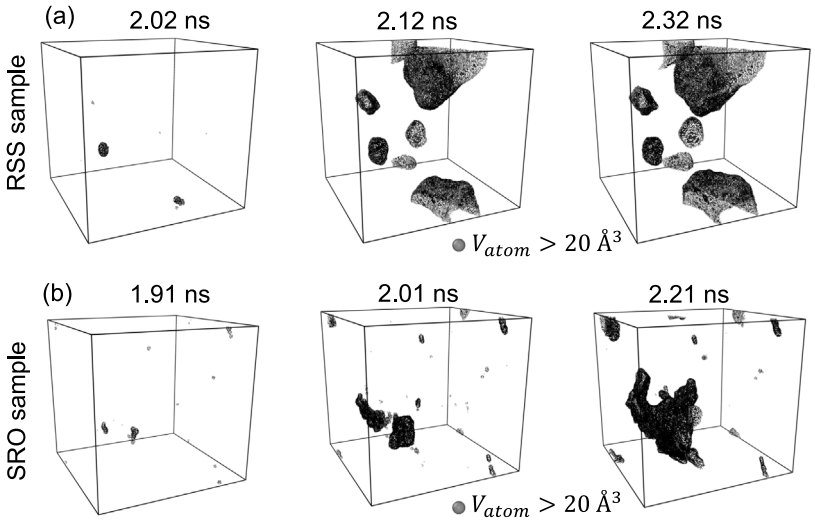


**Fig. 15.** Representative snapshots illustrating void dynamics in (a) RSS and (b) SRO NC samples with the average grain size of 20 nm for the reverse loading ($10^8$ $s^{-1}$) during lp1, respectively. Only void surface atoms are visualized, identified by Voronoi volumes exceeding 20 Å$^3$.

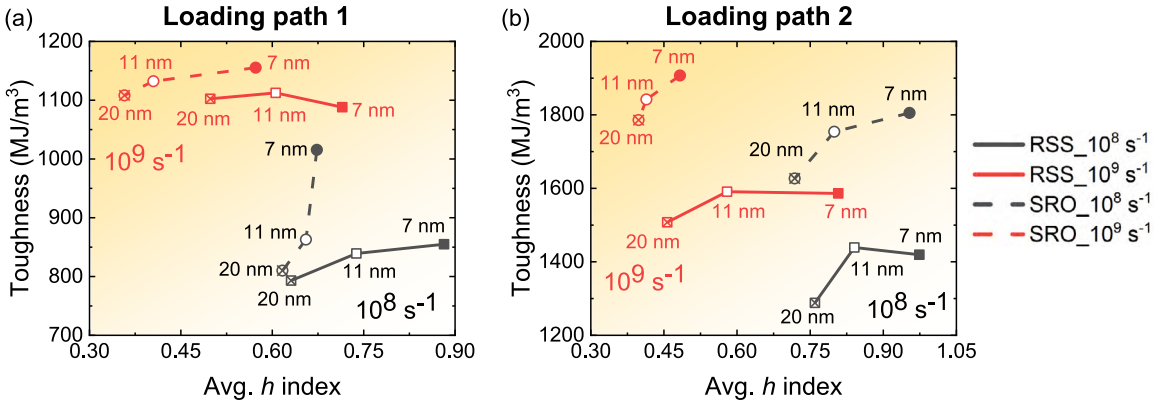


**Fig. 16.** Relation between toughness and the average $h$ index in period I of void evolution in the RSS (solid lines) and SRO (dashed lines) NCs at two strain rates $10^8$ $s^{-1}$ and $10^9$ $s^{-1}$ for (a) lp 1 and (b) lp 2, respectively. The three data points of each sample correspond to the grain sizes of 7, 11, and 20 nm, respectively.

atomic distribution, $h$ equals zero, since $\overline{m}$ and $m_i$ are identical in this scenario. For a given spatial atomic distribution, a higher $h$ value corresponds to an increasing spatial clustering of void-surface atoms and a greater degree of heterogeneity in the distribution. The constant 8.89 limits the maximum value of $h$ to unity [93]. Although the $h$ index is computed over the whole simulation domain, its variation is governed by the occupied-grid population created at GBs, where voids nucleate. The GIs contain negligible void-surface atoms at period I and hence contribute minimally to $h$. Thus, $h$ quantifies the spatial heterogeneity of void formation along the GB network: lower $h$ corresponds to uniformly distributed GB voids, whereas larger $h$ values indicate that voids concentrate in localized GB regions (Figure S19 and S20). Fig. 16 shows the correlation between toughness and the $h$ index. With all else being equal, SRO samples consistently exhibit lower $h$ values than RSS samples, indicating more homogeneous void nucleation along the GB network. This spatial homogenization delays localized void coalescence and correlates with enhanced toughness (Fig. 12).

The link between CSRO and more uniformly distributed void nucleation remains to be clarified. For this purpose, we investigate several nucleation sites in the NC alloys. In SRO alloy, the nucleation sites coincide with the Ni segregation regions, where significant volumetric strain localizes (Fig. 17(b)–(c)), irrespective of grain size and strain rate (see Figure S21 and volumetric strain calculation in *Note* 10 of the supplementary material). This preference for void nucleation at Ni segregation regions in the SRO NC (with a lattice parameter of $a_0$ = 3.565 Å) arises from the lattice mismatch between Ni clusters ($a_0$ = 3.507 Å) and CoCr clusters ($a_0$ = 3.592 Å), which induces tensile residual stresses during reverse loading in the Ni regions and compression stresses in the neighboring CoCr regions [28]. Consequently, cavitation is more likely initiated in the Ni clusters compared to the CoCr clusters. Widespread void nucleation within the CSRO clusters in the GBs gives rise to the relatively uniform distribution of nanovoids that form during the early fracture stage, seen in Fig. 15(b) and characterized by the comparatively low $h$ in Fig. 16.

As straining proceeds, void embryos nucleated at preferential sites such as Ni segregation regions and triple junctions, grow and coalesce along GBs until the cavities link across the material, leading to an intergranular fracture morphology perpendicular to the loading direction (Fig. 17(d)). The energy released by cavitation triggers dislocation emissions in the adjacent FCC GIs, as shown in Fig. 17(d). Consequently, void expansion at GBs, along with dislocation glide in FCC GIs, results in a rapid decrease in CSRO parameters in the later stages of reverse loading for lp1 (Fig. 13(a)). A similar reduction in CSRO is also observed in Fig. 13(b) for lp2, once cavitation begins, due to

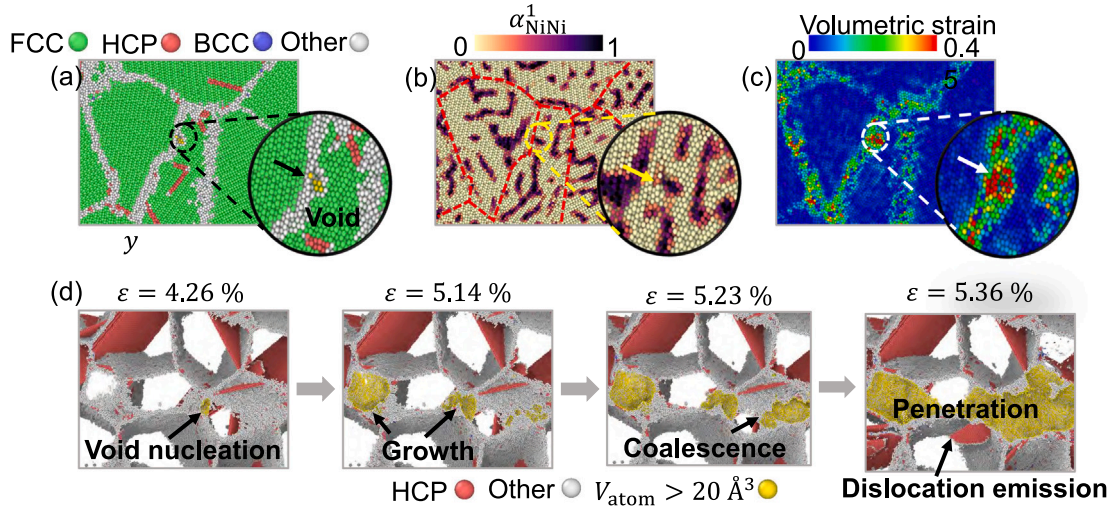


**Fig. 17.** Cavitation process of the SRO NC with the average grain size of $d$ = 20 nm at a strain rate of $10^8$ $s^{-1}$ during the reverse loading of lp1. The loading direction is aligned with the $x$ axis. (a)–(c) Void nucleation and its correlation with the CSRO distribution and volumetric strain field. The red dashed lines in (b) mark the GB locations identified in (a). (d) Evolution of void dynamics, illustrating the processes of nucleation, growth, coalescence, and penetration. The FCC structure is removed for better visualization of defects in GIs. (For interpretation of the references to color in this figure legend, the reader is referred to the web version of this article.)

the destruction of locally ordered clusters by void expansion. Since the FCC phase possesses higher symmetry and a greater number of active slip systems than the HCP phase, allowing it to accommodate plastic deformation more efficiently through dislocation glide. This ductile accommodation delays stress localization and suppresses premature crack propagation. Thus, ductile void growth aided by the FCC phase could explain why more FCC phase than HCP phase at the start of void nucleation (period I) correlates with greater fracture strength.

## 4. Discussion

In nanocrystalline FCC systems, plasticity transitions from dislocation-mediated deformation within GIs to GB-mediated mechanisms as the grain size decreases [78,94]. In this context, CSRO stabilizes GB configurations and reduces their propensity for irreversible atomic rearrangements, thereby increasing the stress required to activate GB-mediated deformation. This stabilization contributes to the observed strengthening. More broadly, the compositional tunability of MPEAs enables the control of GB chemistry through alloying and thermomechanical processing, including local segregation and ordering, which can significantly influence mechanical performance [95–99]. In contrast, LD introduces adversarial effects on the GB activities and plasticity of NC MPEAs. While it can promote dislocation nucleation from GBs and reduce their stability [100], it simultaneously impedes dislocation glide within GIs due to heterogeneous energy barriers [101]. The combined effect of LD therefore leads to a more moderate strengthening compared to CSRO.

The role of CSRO in fracture is closely tied to its influence on void nucleation and growth. Although voids nucleate preferentially at GBs and triple junctions in both RSS and SRO samples, CSRO significantly modifies their spatial distribution and coalescence pathways. In SRO samples, void nucleation occurs more uniformly across the GB network, leading to distributed growth and delayed coalescence. In contrast, RSS samples exhibit more localized void formation, which promotes earlier failure. This behavior is consistent with experimental observations in dynamically loaded CoCrNi alloys [16], where increased interfacial density enhances damage tolerance. Similar concepts of distributed nanovoid formation have also been shown to improve fracture resistance in other systems [102]. These results suggest that CSRO configurations that promote spatially distributed damage evolution are particularly beneficial for dynamic fracture resistance.

Another key aspect revealed in this work is the strong path dependence of CSRO under multi-stage QI loading. The mechanical response is governed not only by the initial CSRO state but also by its evolution during deformation. Under moderate pre-strain (lp1), CSRO is only partially disrupted and retains sufficient connectivity to recover during reverse loading. This partial recovery limits irreversible plastic accommodation and enables sustained reverse loading work, resulting in higher fracture strength and enhanced effective toughness. In contrast, severe pre-strain (lp2) largely destroys CSRO, preventing recovery and leading to highly dissipative deformation dominated by irreversible processes. Consequently, fracture strength and failure strain are reduced, even though the overall toughness remains significant. These findings demonstrate that the dynamic fracture response is intrinsically path-dependent and that the ability of CSRO to persist and recover plays a central role in governing damage tolerance.

From a mechanistic perspective, CSRO also modifies the intragranular deformation mode. Consistent with classical understanding [85,86], CSRO induces glide-plane softening, which alters the slip morphology from intersecting slip networks in the RSS state to more organized arrays of parallel slip bands. This transition leads to macroscopic work softening due to strain localization within individual bands. Although such localization is typically associated with mechanical instability, the concurrent strengthening of GB structures and the modified damage evolution pathways enable CSRO-containing alloys to maintain superior strength and fracture resistance. Furthermore, the HCP-to-BCC phase transformation observed during loading provides an additional mechanism that mitigates excessive softening, suggesting that materials exhibiting phase transformations under dynamic loading may benefit from similar stabilization effects.

Finally, it is important to assess the degree of realism and limitations of the QI loading framework employed here. The imposed uniaxial strain condition approximates the loading state in ramp compression experiment (*Note* 5 in the supplementary material), where rapid deformation suppresses lateral relaxation. This enables the simulations to capture key features of dynamic deformation, including the coupling between mechanical work and microstructural evolution. However, the accessible timescales in the simulations remain significantly shorter than experimental conditions. Despite these limitations, the atomistic framework provides valuable mechanistic insights into the interplay between CSRO, GB-mediated deformation and damage evolution, which

are difficult to isolate experimentally. These insights offer a physically grounded basis for designing MPEAs with improved dynamic mechanical performance through controlled chemical ordering.

## 5. Conclusions

Using a combination of hybrid Monte Carlo/molecular dynamics (MD) and large-scale MD simulations, we perform a three-stage quasi-isentropic (QI) loading procedure (compression-holding-tension scheme) on nanocrystalline (NC) CoCrNi multi-principal element alloys (MPEAs) with different average grain sizes at varied strain rates along two distinct loading paths (lp). The simulations provide insights into the underlying mechanisms of plastic deformation and dynamic fracture evolution, with a particular focus on grain boundary (GB) behavior. The main findings are summarized as follows:

- Under QI compression, CoCrNi MPEA with random atomic distribution exhibits reduced yield strength with decreasing grain size. This phenomenon is attributed to enhanced GB relaxation caused by more severe grain rotation in samples with smaller grains. Introducing chemical short-range order (CSRO) into GBs and grain interiors (GIs) lowers GB potential energy and suppresses both grain rotation and GB displacement, thereby increasing yield strength and weakening the grain size dependence.
- Larger grain sizes facilitate dislocation multiplication within GIs, which aids in GB displacement. In samples with CSRO, however, preferential coplanar slip leads to progressive degradation of CSRO in a loading-history-dependent manner. During reverse loading, the partially destructed CSRO is able to recover through reversible dislocation activities, contributing to the rejuvenation of the material. The rejuvenation capability can be lost when extensive plastic deformation induces an unrecoverable CSRO destruction.
- Greater GB displacements in NC samples with larger grain sizes destabilize GB structures during initial deformation and promote earlier intergranular void nucleation, consequently reducing fracture strength. Fracture strength demonstrates positive strain-rate sensitivity, while the grain size effect on fracture strength diminishes at higher strain rates due to the increased frequency of void nucleation and the accelerated expansion of voids.
- Although CSRO promotes void nucleation at GBs due to the stress/strain concentration induced by lattice misfit, the resulting uniformly dispersed void embryos form rough fracture profiles through rugged void connection paths. This hinders void expansion and retards damage accumulation during intergranular fracture, thereby improving the damage resistance of the material.
- The dynamic fracture response of CoCrNi under QI multi-stage loading is strongly path-dependent, and the ability of CSRO to survive and rejuvenate during reverse loading governs the balance between irreversible work and recoverable work. Partial CSRO retention along lp1 enables rejuvenation and enhances fracture strength and toughness, whereas severe CSRO destruction for lp2 suppresses rejuvenation, increases irreversible work, and degrades strength and failure strain despite maintaining high toughness.

## CRediT authorship contribution statement

**Zhuocheng Xie:** Writing – review & editing, Writing – original draft, Visualization, Software, Methodology, Investigation, Formal analysis, Data curation, Conceptualization. **Wu-Rong Jian:** Writing – review & editing, Visualization, Validation, Software, Methodology, Investigation, Formal analysis, Funding acquisition, Supervision, Conceptualization. **Shuozhi Xu:** Writing – review & editing, Methodology, Formal analysis, Data curation. **Irene J. Beyerlein:** Writing – review & editing, Methodology, Formal analysis. **Xiaoqing Zhang:** Writing – review & editing, Funding acquisition, Formal analysis. **Ningbo Zhang:** Validation, Formal analysis. **Xiaohu Yao:** Writing – review & editing, Funding acquisition, Formal analysis, Conceptualization.

## Declaration of competing interest

The authors declare the following financial interests/personal relationships which may be considered as potential competing interests: The co-author Irene J. Beyerlein is an Editor for Acta Materialia and was not involved in the editorial review or the decision to publish this article.

## Acknowledgements

This work is partially supported by High Performance Computing Platform of South China University of Technology. Z.X. acknowledges support from the National Natural Science Foundation of China (No. U2441214). X.Y. would like to express his sincere gratitude for the financial support from the National Natural Science Foundation of China (No. 12232006). X.Z. acknowledges support from the National Natural Science Foundation of China (No. 12472382). W.J. acknowledges support from the Natural Science Fund for Excellent Young Scholar of Guangdong Province, China (No. 2026A1515030015).

## Appendix A. Supplementary data

Supplementary material including additional methods, data, and analyses supporting the results presented in this paper can be found online at https://doi.org/10.1016/j.actamat.2026.122263.

## References

[1] Z. Li, S. Zhao, R.O. Ritchie, M.A. Meyers, Mechanical properties of high-entropy alloys with emphasis on face-centered cubic alloys, Prog. Mater. Sci. 102 (2019) 296–345.
[2] W. Li, D. Xie, D. Li, Y. Zhang, Y. Gao, P.K. Liaw, Mechanical behavior of high-entropy alloys, Prog. Mater. Sci. (2021) 100777.
[3] Y. Tang, R. Wang, B. Xiao, Z. Zhang, S. Li, J. Qiao, S. Bai, Y. Zhang, P.K. Liaw, A review on the dynamic-mechanical behaviors of high-entropy alloys, Prog. Mater. Sci. 135 (2023) 101090.
[4] Z. Jiang, J. He, H. Wang, H. Zhang, Z. Lu, L. Dai, Shock compression response of high entropy alloys, Mater. Res. Lett. 4 (4) (2016) 226–232.
[5] N. Zhang, J. Xu, Z. Feng, Y. Sun, J. Huang, X. Zhao, X. Yao, S. Chen, L. Lu, S. Luo, Shock compression and spallation damage of high-entropy alloy $Al_{0.1}$CoCrFeNi, J. Mater. Sci. Technol. 128 (2022) 1–9.
[6] Y. Yang, S. Yang, H. Wang, Effects of the phase content on dynamic damage evolution in $Fe_{50}Mn_{30}Co_{10}Cr_{10}$ high entropy alloy, J. Alloys Compd. 851 (2020) 156883.
[7] Y. Yang, S. Yang, H. Wang, Effects of microstructure on the evolution of dynamic damage of $Fe_{50}Mn_{30}Co_{10}Cr_{10}$ high entropy alloy, Mater. Sci. Eng. A (2020) 140440.
[8] A. Cui, S. Hu, S. Zhang, J. Cheng, Q. Li, J. Huang, S. Luo, Spall response of medium-entropy alloy CrCoNi under plate impact, Int. J. Mech. Sci. 252 (2023) 108331.
[9] J. Cheng, H. Qin, C. Li, F. Zhao, R. Pan, Q. Wang, Y. Bian, S. Luo, Deformation and damage of equiatomic CoCrFeNi high-entropy alloy under plate impact loading, Mater. Sci. Eng. A 862 (2023) 144432.
[10] J.-W. Yeh, S.-K. Chen, S.-J. Lin, J.-Y. Gan, T.-S. Chin, T.-T. Shun, C.-H. Tsau, S.-Y. Chang, Nanostructured high-entropy alloys with multiple principal elements: novel alloy design concepts and outcomes, Adv. Eng. Mater. 6 (5) (2004) 299–303.
[11] B. Cantor, I. Chang, P. Knight, A. Vincent, Microstructural development in equiatomic multicomponent alloys, Mater. Sci. Eng. A 375 (2004) 213–218.
[12] B. Cantor, Multicomponent high-entropy cantor alloys, Prog. Mater. Sci. 120 (2021) 100754.
[13] R.O. Ritchie, The conflicts between strength and toughness, Nat. Mater. 10 (11) (2011) 817–822.
[14] N. Yan, Z. Li, Y. Xu, M.A. Meyers, Shear localization in metallic materials at high strain rates, Prog. Mater. Sci. 119 (2021) 100755.
[15] J. Cheng, J. Xu, X. Zhao, K. Shi, J. Li, Q. Zhang, J. Qiao, J. Huang, S. Luo, Shock compression and spallation of a medium-entropy alloy $Fe_{40}Mn_{20}Cr_{20}Ni_{20}$, Mater. Sci. Eng. A 847 (2022) 143311.

[16] S. Zhao, S. Yin, X. Liang, F. Cao, Q. Yu, R. Zhang, L. Dai, C.J. Ruestes, R.O. Ritchie, A.M. Minor, Deformation and failure of the CrCoNi medium-entropy alloy subjected to extreme shock loading, Sci. Adv. 9 (18) (2023) eadf8602.

[17] N. Zhang, Z. Tang, Z. Lin, S. Zhu, Y. Cai, S. Chen, L. Lu, X. Zhao, S. Luo, Deformation and damage of heterogeneous-structured high-entropy alloy CrMnFeCoNi under plate impact, Mater. Sci. Eng. A. 843 (2022) 143069.

[18] S. Zhao, Z. Li, C. Zhu, W. Yang, Z. Zhang, D.E. Armstrong, P.S. Grant, R.O. Ritchie, M.A. Meyers, Amorphization in extreme deformation of the CrMnFeCoNi high-entropy alloy, Sci. Adv. 7 (5) (2021) eabb3108.

[19] M.A. Meyers, Dynamic Behavior of Materials, John wiley & sons, 1994.

[20] K. Jiang, T. Ren, G. Shan, T. Ye, L. Chen, C. Wang, F. Zhao, J. Li, T. Suo, Dynamic mechanical responses of the Al0.1CoCrFeNi high entropy alloy at cryogenic temperature, Mater. Sci. Eng. A 797 (2020) 140125.

[21] L. Wang, J. Qiao, S. Ma, Z. Jiao, T. Zhang, G. Chen, D. Zhao, Y. Zhang, Z. Wang, Mechanical response and deformation behavior of Al0.6CoCrFeNi high-entropy alloys upon dynamic loading, Mater. Sci. Eng. A 727 (2018) 208–213.

[22] J. He, Q. Wang, H. Zhang, L. Dai, T. Mukai, Y. Wu, X. Liu, H. Wang, T.-G. Nieh, Z. Lu, Dynamic deformation behavior of a face-centered cubic FeCoNiCrMn high-entropy alloy, Sci. Bull. 63 (6) (2018) 362–368.

[23] N. Kumar, Q. Ying, X. Nie, R. Mishra, Z. Tang, P. Liaw, R. Brennan, K. Doherty, K. Cho, High strain-rate compressive deformation behavior of the Al0.1CrFeCoNi high entropy alloy, Mater. Des. 86 (2015) 598–602.

[24] D. Foley, S. Huang, E. Anber, L. Shanahan, Y. Shen, A. Lang, C. Barr, D. Spearot, L. Lamberson, M. Taheri, Simultaneous twinning and microband formation under dynamic compression in a high entropy alloy with a complex energetic landscape, Acta Mater. 200 (2020) 1–11.

[25] F. Zhang, Y. Ren, Z. Pei, Q. Gao, Z. Lu, B. Wang, Y. Xue, X. Cao, K. Du, Y. Yang, et al., Cooperative dislocations for pressure-dependent sequential deformation of multi-principal element alloys under shock loading, Acta Mater. 276 (2024) 120150.

[26] K. Yang, Z. Feng, X. Zhao, J. Li, J. Huang, Phase transitions in additively manufactured high-entropy alloy $Cr_{10}Mn_{10}Fe_{60}Co_{10}Ni_{10}$ induced by high strain rate compression, Scr. Mater. 221 (2022) 114955.

[27] Y. Zhang, N. Zhang, Y. Tang, Y. Cai, L. Lu, S. Luo, Multiple phase transitions in shock compressed high-entropy alloy $Cr_9Mn_9Fe_64Co_9Ni_9$: Experiments and molecular dynamics simulations, Appl. Phys. Lett. 124 (10) (2024).

[28] Z. Xie, W.-R. Jian, S. Xu, I.J. Beyerlein, X. Zhang, Z. Wang, X. Yao, Role of local chemical fluctuations in the shock dynamics of medium entropy alloy CoCrNi, Acta Mater. 221 (2021) 117380.

[29] W.-R. Jian, Z. Xie, S. Xu, X. Yao, I.J. Beyerlein, Shock-induced amorphization in medium entropy alloy CoCrNi, Scr. Mater. 209 (2022) 114379.

[30] K. Wang, L. Feng, X. Zou, G. Huang, W.-R. Jian, S. Qin, Z. Xie, X. Yao, Shock response of gradient nanocrystalline CoCrNi medium entropy alloy, Int. J. Mech. Sci. 280 (2024) 109498.

[31] X. Yang, T. Lu, X. Li, C. He, X.-C. Zhang, H. Chen, S.-T. Tu, Microstructural effects on shock-induced deformation behavior in CoCrNi medium-entropy alloy: A molecular dynamics study, J. Mater. Sci. Technol. 229 (2025) 309–320.

[32] Q. Liu, J. Hua, Y. Xu, K. Yang, J. Cheng, N. Zhang, C. Li, Y. Cai, S. Luo, Ballistic penetration of high-entropy CrMnFeCoNi alloy: Experiments and modelling, Int. J. Mech. Sci. 249 (2023) 108252.

[33] A. Tamm, A. Aabloo, M. Klintenberg, M. Stocks, A. Caro, Atomic-scale properties of Ni-based FCC ternary, and quaternary alloys, Acta Mater. 99 (2015) 307–312.

[34] F. Zhang, S. Zhao, K. Jin, H. Xue, G. Velisa, H. Bei, R. Huang, J. Ko, D. Pagan, J. Neuefeind, et al., Local structure and short-range order in a NiCoCr solid solution alloy, Phys. Rev. Lett. 118 (20) (2017) 205501.

[35] J. Ding, Q. Yu, M. Asta, R.O. Ritchie, Tunable stacking fault energies by tailoring local chemical order in CrCoNi medium-entropy alloys, Proc. Natl. Acad. Sci. 115 (36) (2018) 8919–8924.

[36] F. Walsh, M. Asta, R.O. Ritchie, Magnetically driven short-range order can explain anomalous measurements in CrCoNi, Proc. Natl. Acad. Sci. 118 (13) (2021) e2020540118.

[37] S. Moniri, Y. Yang, J. Ding, Y. Yuan, J. Zhou, L. Yang, F. Zhu, Y. Liao, Y. Yao, L. Hu, et al., Three-dimensional atomic structure and local chemical order of medium-and high-entropy nanoalloys, Nature 624 (7992) (2023) 564–569.

[38] M. He, W.J. Davids, A.J. Breen, S.P. Ringer, Quantifying short-range order using atom probe tomography, Nat. Mater. (2024) 1–8.

[39] Y. Yang, S. Yin, Q. Yu, Y. Zhu, J. Ding, R. Zhang, C. Ophus, M. Asta, R.O. Ritchie, A.M. Minor, Rejuvenation as the origin of planar defects in the CrCoNi medium entropy alloy, Nat. Commun. 15 (1) (2024) 1402.

[40] M.A. Meyers, C.T. Aimone, Dynamic fracture (spalling) of metals, Prog. Mater. Sci. 28 (1) (1983) 1–96.

[41] T.P. Remington, B.A. Remington, E.N. Hahn, M.A. Meyers, Deformation and failure in extreme regimes by high-energy pulsed lasers: A review, Mater. Sci. Eng. A 688 (2017) 429–458.

[42] K. Lorenz, M. Edwards, A. Jankowski, S. Pollaine, R. Smith, B. Remington, High pressure, quasi-isentropic compression experiments on the omega laser, High Energy Density Phys. 2 (3–4) (2006) 113–125.

[43] H. Jarmakani, J. McNaney, B. Kad, D. Orlikowski, J. Nguyen, M. Meyers, Dynamic response of single crystalline copper subjected to quasi-isentropic, gas-gun driven loading, Mater. Sci. Eng. A 463 (1–2) (2007) 249–262.

[44] T. Vogler, T. Ao, J.R. Asay, High-pressure strength of aluminum under quasi-isentropic loading, Int. J. Plast. 25 (4) (2009) 671–694.

[45] C. Seagle, J.-P. Davis, M. Martin, H. Hanshaw, Shock-ramp compression: Ramp compression of shock-melted tin, Appl. Phys. Lett. 102 (24) (2013) 244104.

[46] B. Luo, X. Chen, G. Wang, F. Tan, G. Chen, J. Zhao, C. Sun, Dynamic strength measurement of aluminum under magnetically driven ramp wave pressure-shear loading, Int. J. Impact Eng. 100 (2017) 56–61.

[47] A. Higginbotham, J. Hawreliak, E. Bringa, G. Kimminau, N. Park, E. Reed, B. Remington, J. Wark, Molecular dynamics simulations of ramp-compressed copper, Phys. Rev. B 85 (2) (2012) 024112.

[48] Y. Cai, L. Wang, H. Wu, M. Zhu, C. Liu, S. Luo, Homogeneous crystal nucleation in liquid copper under quasi-isentropic compression, Phys. Rev. B 92 (1) (2015) 014108.

[49] J.M.D. Lane, S.M. Foiles, H. Lim, J.L. Brown, Strain-rate dependence of ramp-wave evolution and strength in tantalum, Phys. Rev. B 94 (6) (2016) 064301.

[50] M. Xiang, J. Chen, R. Su, Spalling behaviors of Pb induced by ramp-wave-loading: Effects of the loading rise time studied by molecular dynamics simulations, Comput. Mater. Sci. 117 (2016) 370–379.

[51] K. Wang, J. Chen, W. Zhu, W. Hu, M. Xiang, Phase transition of iron-based single crystals under ramp compressions with extreme strain rates, Int. J. Plast. 96 (2017) 56–80.

[52] Z. Xie, W.-R. Jian, S. Xu, I.J. Beyerlein, X. Zhang, X. Yao, R. Zhang, Phase transition in medium entropy alloy CoCrNi under quasi-isentropic compression, Int. J. Plast. 157 (2022) 103389.

[53] R. Zhang, S. Zhao, J. Ding, Y. Chong, T. Jia, C. Ophus, M. Asta, R.O. Ritchie, A.M. Minor, Short-range order and its impact on the CrCoNi medium-entropy alloy, Nature 581 (7808) (2020) 283–287.

[54] B. Yin, S. Yoshida, N. Tsuji, W. Curtin, Yield strength and misfit volumes of NiCoCr and implications for short-range-order, Nat. Commun. 11 (1) (2020) 2507.

[55] D. Liu, Q. Yu, S. Kabra, M. Jiang, P. Forna-Kreutzer, R. Zhang, M. Payne, F. Walsh, B. Gludovatz, M. Asta, et al., Exceptional fracture toughness of CrCoNi-based medium-and high-entropy alloys at 20 kelvin, Science 378 (6623) (2022) 978–983.

[56] A.P. Thompson, H.M. Aktulga, R. Berger, D.S. Bolintineanu, W.M. Brown, P.S. Crozier, P.J. In't Veld, A. Kohlmeyer, S.G. Moore, T.D. Nguyen, et al., LAMMPS-a flexible simulation tool for particle-based materials modeling at the atomic, meso, and continuum scales, Comput. Phys. Comm. 271 (2022) 108171.

[57] Q.-J. Li, H. Sheng, E. Ma, Strengthening in multi-principal element alloys with local-chemical-order roughened dislocation pathways, Nat. Commun. 10 (1) (2019) 1–11.

[58] F.-H. Cao, Y.-J. Wang, L.-H. Dai, Novel atomic-scale mechanism of incipient plasticity in a chemically complex CrCoNi medium-entropy alloy associated with inhomogeneity in local chemical environment, Acta Mater. (2020).

[59] W.-R. Jian, Z. Xie, S. Xu, Y. Su, X. Yao, I.J. Beyerlein, Effects of lattice distortion and chemical short-range order on the mechanisms of deformation in medium entropy alloy CoCrNi, Acta Mater. 199 (2020) 352–369.

[60] P. Cao, Maximum strength and dislocation patterning in multi–principal element alloys, Sci. Adv. 8 (45) (2022) eabq7433.

[61] L. Zhu, X. Zhang, W.-R. Jian, Z. Xie, X. Yao, Plastic deformation mechanism and defect patterning under nanoindentation in medium entropy alloy CoCrNi, J. Alloys Compd. 968 (2023) 171734.

[62] G. Huang, X. Zhang, R. Zhang, W.-R. Jian, X. Zou, K. Wang, Z. Xie, X. Yao, The shear softening and dislocation glide competition due to the shear-induced short-range order degeneration in CoCrNi medium-entropy alloy, J. Mater. Sci. Technol. (2024).

[63] F. Cao, Y. Chen, S. Zhao, E. Ma, L. Dai, Grain boundary phase transformation in a CrCoNi complex concentrated alloy, Acta Mater. 209 (2021) 116786.

[64] S. Sun, Y. Yang, C. Han, G. Sun, Y. Chen, H. Zong, J. Hu, S. Han, X. Liao, X. Ding, et al., Unveiling the grain boundary-related effects on the incipient plasticity and dislocation behavior in nanocrystalline CrCoNi medium-entropy alloy, J. Mater. Sci. Technol. 127 (2022) 98–107.

[65] F. Cao, Y. Chen, H.-Y. Wang, L.-H. Dai, Chemical inhomogeneity inhibits grain boundary fracture: A comparative study in CrCoNi medium entropy alloy, J. Mater. Sci. Technol. 153 (2023) 228–241.

[66] W. Brostow, J.-P. Dussault, B.L. Fox, Construction of voronoi polyhedra, J. Comput. Phys. 29 (1) (1978) 81–92.

[67] E.N. Hahn, T.C. Germann, R. Ravelo, J.E. Hammerberg, M.A. Meyers, On the ultimate tensile strength of tantalum, Acta Mater. 126 (2017) 313–328.

[68] J. Dong, X. Zhang, G. Wang, X. Wu, B. Luo, X. Chen, F. Tan, J. Zhao, C. Sun, Mechanical responses and crystal plasticity model of CoCrNi medium-entropy alloy under ramp wave compression, Matter Radiat. At Extrem. 9 (5) (2024).

[69] A. Stukowski, V.V. Bulatov, A. Arsenlis, Automated identification and indexing of dislocations in crystal interfaces, Modelling Simul. Mater. Sci. Eng. 20 (8) (2012) 085007.

[70] A. Stukowski, Visualization and analysis of atomistic simulation data with OVITO–the Open Visualization Tool, Modelling Simul. Mater. Sci. Eng. 18 (1) (2009) 015012.

[71] D.L. Olmsted, S.M. Foiles, E.A. Holm, Survey of computed grain boundary properties in face-centered cubic metals: I. Grain boundary energy, Acta Mater. 57 (13) (2009) 3694–3703.
[72] T. Frolov, M. Asta, Y. Mishin, Segregation-induced phase transformations in grain boundaries, Phys. Rev. B 92 (2) (2015) 020103.
[73] A. Stukowski, Computational analysis methods in atomistic modeling of crystals, JOM 66 (3) (2014) 399–407.
[74] J. Cowley, An approximate theory of order in alloys, Phys. Rev. 77 (5) (1950) 669.
[75] D. de Fontaine, The number of independent pair-correlation functions in multicomponent systems, J. Appl. Crystal. 4 (1) (1971) 15–19.
[76] J. Schiøtz, F.D. Di Tolla, K.W. Jacobsen, Softening of nanocrystalline metals at very small grain sizes, Nature 391 (6667) (1998) 561–563.
[77] D. Wolf, V. Yamakov, S. Phillpot, A. Mukherjee, H. Gleiter, Deformation of nanocrystalline materials by molecular-dynamics simulation: Relationship to experiments, Acta Mater. 53 (1) (2005) 1–40.
[78] E.N. Hahn, M.A. Meyers, Grain-size dependent mechanical behavior of nanocrystalline metals, Mater. Sci. Eng. A 646 (2015) 101–134.
[79] M.L. Falk, J.S. Langer, Dynamics of viscoplastic deformation in amorphous solids, Phys. Rev. E. 57 (6) (1998) 7192.
[80] L. Wang, J. Teng, P. Liu, A. Hirata, E. Ma, Z. Zhang, M. Chen, X. Han, Grain rotation mediated by grain boundary dislocations in nanocrystalline platinum, Nat. Commun. 5 (1) (2014) 4402.
[81] B. Chen, K. Lutker, J. Lei, J. Yan, S. Yang, H.-k. Mao, Detecting grain rotation at the nanoscale, Proc. Natl. Acad. Sci. 111 (9) (2014) 3350–3353.
[82] E.C. Bain, N. Dunkirk, The nature of martensite, Trans. Am. Inst. Min. Met. Eng. 70 (1) (1924) 25–47.
[83] Z. Nishiyama, Martensitic Transformation, Elsevier, 2012.
[84] H. He, M. Naeem, F. Zhang, Y. Zhao, S. Harjo, T. Kawasaki, B. Wang, X. Wu, S. Lan, Z. Wu, et al., Stacking fault driven phase transformation in CrCoNi medium entropy alloy, Nano Lett. 21 (3) (2021) 1419–1426.
[85] N. Clement, D. Caillard, J. Martin, Heterogeneous deformation of concentrated Ni-Cr FCC alloys: Macroscopic and microscopic behaviour, Acta Metall. 32 (6) (1984) 961–975.
[86] V. Gerold, H. Karnthaler, On the origin of planar slip in fcc alloys, Acta Metall. 37 (8) (1989) 2177–2183.
[87] R.D. White, B. Ahmadikia, I.J. Beyerlein, Grain size effects on slip band development, Int. J. Solids Struct. (2025) 113589.
[88] Y. Jo, W. Choi, D. Kim, A. Zargaran, S.S. Sohn, H.S. Kim, B. Lee, N.J. Kim, S. Lee, FCC to BCC transformation-induced plasticity based on thermodynamic phase stability in novel $V_{10}Cr_{10}Fe_{45}Co_xNi_{35}$-x medium-entropy alloys, Sci. Rep. 9 (1) (2019) 1–14.
[89] J.W. Bae, J.B. Seol, J. Moon, S.S. Sohn, M.J. Jang, H.Y. Um, B.-J. Lee, H.S. Kim, Exceptional phase-transformation strengthening of ferrous medium-entropy alloys at cryogenic temperatures, Acta Mater. 161 (2018) 388–399.
[90] H. Shahmir, P. Asghari-Rad, M.S. Mehranpour, F. Forghani, H.S. Kim, M. Nili-Ahmadabadi, Evidence of FCC to HCP and BCC-martensitic transformations in a CoCrFeNiMn high-entropy alloy by severe plastic deformation, Mater. Sci. Eng. A 807 (2021) 140875.
[91] L. Li, Z. Chen, S. Kuroiwa, M. Ito, K. Yuge, K. Kishida, H. Tanimoto, Y. Yu, H. Inui, E.P. George, Evolution of short-range order and its effects on the plastic deformation behavior of single crystals of the equiatomic Cr-Co-Ni medium-entropy alloy, Acta Mater. 243 (2023) 118537.
[92] Q. Fang, Y. Chen, J. Li, C. Jiang, B. Liu, Y. Liu, P.K. Liaw, Probing the phase transformation and dislocation evolution in dual-phase high-entropy alloys, Int. J. Plast. 114 (2019) 161–173.
[93] H.-K. Kim, M. Lee, K.-R. Lee, J.-C. Lee, How can a minor element added to a binary amorphous alloy simultaneously improve the plasticity and glass-forming ability? Acta Mater. 61 (17) (2013) 6597–6608.
[94] M.A. Meyers, A. Mishra, D.J. Benson, Mechanical properties of nanocrystalline materials, Prog. Mater. Sci. 51 (4) (2006) 427–556.
[95] Z. Wu, W. Guo, K. Jin, J.D. Poplawsky, Y. Gao, H. Bei, Enhanced strength and ductility of a tungsten-doped CoCrNi medium-entropy alloy, J. Mater. Res. 33 (19) (2018) 3301–3309.
[96] J. He, S.K. Makineni, W. Lu, Y. Shang, Z. Lu, Z. Li, B. Gault, On the formation of hierarchical microstructure in a Mo-doped NiCoCr medium-entropy alloy with enhanced strength-ductility synergy, Scr. Mater. 175 (2020) 1–6.
[97] Y. Zhao, T. Yang, Y. Tong, J. Wang, J. Luan, Z. Jiao, D. Chen, Y. Yang, A. Hu, C. Liu, et al., Heterogeneous precipitation behavior and stacking-fault-mediated deformation in a CoCrNi-based medium-entropy alloy, Acta Mater. 138 (2017) 72–82.
[98] Y. Zhao, Z. Lei, Z. Lu, J. Huang, T. Nieh, A simplified model connecting lattice distortion with friction stress of Nb-based equiatomic high-entropy alloys, Mater. Res. Lett. 7 (8) (2019) 340–346.
[99] N. An, Y. Sun, Y. Wu, J. Tian, Z. Li, Q. Li, J. Chen, X. Hui, High temperature strengthening via nanoscale precipitation in wrought CoCrNi-based medium-entropy alloys, Mater. Sci. Eng. A. 798 (2020) 140213.
[100] D. Hua, Q. Zhou, Y. Shi, S. Li, K. Hua, H. Wang, S. Li, W. Liu, Revealing the deformation mechanisms of <110> symmetric tilt grain boundaries in CoCrNi medium-entropy alloy, Int. J. Plast. 171 (2023) 103832.
[101] D. Utt, S. Lee, Y. Xing, H. Jeong, A. Stukowski, S.H. Oh, G. Dehm, K. Albe, The origin of jerky dislocation motion in high-entropy alloys, Nat. Commun. 13 (1) (2022) 4777.
[102] J.-J. Chen, H. Xie, L.-Z. Liu, H. Guan, Z. You, L. Zou, H.-J. Jin, Strengthening gold with dispersed nanovoids, Science 385 (6709) (2024) 629–633.